INTERNATIONAL JOURNAL FOR NUMERICAL METHODS IN FLUIDS
Int. J. Numer. Meth. Fluids **31**: 1221–1264 (1999)

A MULTI-LEVEL ADAPTATION MODEL OF CIRCULATION FOR THE WESTERN INDIAN OCEAN

C. SHAJI[a,*], N. BAHULAYAN[b], S.K. DUBE[a] AND A.D. RAO[a]

[a] *Centre for Atmospheric Sciences, Indian Institute of Technology, Hauz Khas, New Delhi 110016, India*
[b] *Physical Oceanography Division, National Institute of Oceanography, Dona Paula, Goa 403004, India*

SUMMARY

A three-dimensional, fully non-linear semi-diagnostic (adaptation) model is described. This model is used to compute the climatological mean circulation and to understand the role of local, steady forcing of the wind and thermohaline forcing on the observed circulation in the western tropical Indian Ocean. The model consists of equations of motion and continuity, sea surface topography, equations of state and temperature, and salinity diffusion equations. While the sea surface topography equation is solved by a successive overrelaxation technique, the other model equations are solved by a leap-frog numerical scheme. Two versions of the model, having 18 and 33 levels in the vertical direction, were prepared to study climatological mean circulation in the western tropical Indian Ocean. The first numerical experiment is carried out with the 18-level adaptation model to study the sensitivity of the solution to different values of eddy coefficients. The main scientific rationale behind these numerical experiments was to obtain the most appropriate values of the eddy coefficients for the realistic computation of climatological circulation in the western tropical Indian Ocean. Three numerical experiments were conducted for the month of February to understand the sensitivity of the model solution to different eddy coefficients. The model reproduced the circulation features during February, even with low values of horizontal and vertical eddy coefficients. In the second experiment, the adaptation model, with 33 levels in the vertical direction, is applied to study the seasonal mean climatological circulation at selected depths during Spring in the western tropical Indian Ocean. Adapted (steady state) results of currents, sea surface topography, temperature and salinity anomaly fields are presented. Reasonable agreement is obtained between the model results on currents and the observational data. The computed anomaly fields for temperature and salinity at selected depths during Spring show that the observed temperature and salinity data were adapted with surface wind, flow field and bottom relief of the ocean and that the observed data were found to be fully smoothed during the adaptation stage. Copyright © 1999 John Wiley & Sons, Ltd.

KEY WORDS: adaptation model; climatic circulation; sea surface topography; thermohaline forcing; open boundary condition

1. INTRODUCTION

The three-dimensional circulation on basin scales is always computed from indirect observations of oceanic properties, especially observations on temperature and salinity. In the early 1950s, the dynamic method was commonly used for the computation of density-driven circulation (gradient currents) in the sea. This method has a number of drawbacks: it computes only the relative currents under the assumption that the flow field is zero at some lower levels.

* Correspondence to: Centre for Atmospheric Sciences, Indian Institute of Technology, Hauz Khas, New Delhi 110016, India.

CCC 0271–2091/99/241221–44$17.50

Received July 1998
Revised October 1998

In the real ocean, the vertical profile of gradient flow may behave quite arbitrarily; at some depth, the flow direction changes sign, while at some other depth it decreases slowly or increases abruptly. There is no zero-velocity level in the real ocean that could be taken as a reference level. In addition, the dynamic method does not take into account the direct effect of tangential wind stress and bottom topography. The upper level circulation in the ocean is mainly controlled by wind stress forcing and hence it is necessary to develop alternate methods for the computation of three-dimensional circulation that take into account wind stress, thermohaline forcing and bottom topography. One of the methods normally used to study three-dimensional circulation in the ocean, considering wind field and thermohaline forcing, is the diagnostic method. In a diagnostic model, primitive equations of momentum, hydrostatics and continuity are integrated with appropriate boundary and initial conditions, using observed density and wind stress forcing parameters. Since density is directly imposed on the model from observations of temperature and salinity, there is no need to include the equation of state and turbulent diffusion equations of heat and salt in the diagnostic model. The equation of state is used to derive the density field and the density is kept constant throughout the model integration. In addition to the above-mentioned equations, one equation in terms of mass transport streamfunction or sea surface topography is also included in diagnostic models.

Many diagnostic calculations of seasonal mean currents in the non-equatorial regions of the world oceans have been carried out by Sarkisyan and his co-workers [1–4]. These calculations show that, on average, the baroclinic currents do not decay very rapidly with depth. Even at greater depths, the horizontal gradient of density is one of the main factors that control the large scale circulation in the ocean. Mellor *et al.* [5] has carried out the diagnostic calculation of the general circulation of Atlantic Ocean using low-Rossby number equations of motion, where all frictional terms except surface wind stress were neglected. Climatological surface wind stress, temperature, salinity and bottom topography were used as input data to the calculation. Despite the coarse resolution ($1° \times 1°$) used in the model, the results showed considerable details of the circulation, particularly in the higher latitude regions of the Atlantic Ocean. Kantha *et al.* [6] developed a diagnostic model for the calculation of circulation in the South Atlantic Bight. The diagnostic calculation involved the integration of geostrophic equation for total transport along contours of constant planetary vorticity. In the above model, authors have neglected both advection and diffusion terms in the momentum equations and also in the resultant vorticity balance. The results of the calculation indicated realistic climatological Gulf Stream behaviour in the South Atlantic Bight. Sarmiento and Bryan [7] also developed a robust diagnostic model for the Atlantic Ocean which incorporated the conservation equations of heat and salt as well as momentum. They added damping terms on the right-hand side of the conservation equations for temperature and salinity. The horizontal circulation calculated from this model was consistent with the geostrophic currents expected from observed density field. However, the sources and sinks of salt and heat created by the damping terms were large enough to distort the heat and salt budgets in several regions of the model.

The diagnostic calculations have two significant disadvantages: firstly, the input of density field (temperature and salinity) always contains 'noise' effects of non-stationary processes and motions of small subgrid-scale (SGS), especially synoptic-scale motions. This would lead to distortions in the field of climatic currents to be calculated. Secondly, the specified density fields do not correlate with bottom topography and wind field. In view of the above facts, it is essential to design numerical models and to develop techniques that would provide mutually adjusted hydrological fields. These mutually adjusted hydrological fields, on the one hand, are similar to observed data and, on the other, are well adjusted hydrodynamically without small

scale 'noises'. Semi-diagnostic circulation models are effective tools for obtaining mutually adjusted hydrological fields. The concept and basic approach to semi-diagnostic modelling were first developed by Sarkisyan and Demin [8]. Marchuk and Sarkisyan [9] published a brief analysis of the results of the semi-diagnostic calculation of currents in the North Atlantic and Black Sea areas.

Herein, a three-dimensional semi-diagnostic (adaptation) model is described and the same is used for numerical experimentation to compute the circulation in the western part of tropical Indian Ocean. Firstly, sensitivity experiments were carried out with the model to study the sensitivity of the solution to different values of horizontal and vertical eddy viscosity/diffusivity coefficients. Based on these experiments, the most appropriate values of these coefficients for the realistic calculation of climatological circulation in the western tropical Indian Ocean is fixed. In the second experiment, the numerical model is used to obtain hydrodynamically adjusted fields of currents, temperature and salinity during Spring.

2. FORMULATION OF THE MODEL

2.1. Governing equations

The basic hydrothermodynamic equations of the model is based upon the dynamical framework described by Gill [10], consisting of the equations for the exchange of momentum, mass, heat and salt. These equations are supplemented by the sea surface topography (sea level) equation. Scale analysis of the governing equations shows that non-linear and friction terms have the same order of magnitude and both play a major role in the dynamics of circulation in the equatorial regions, where geostrophy fails. The present model differs from the classical primitive equation models in two aspects: (1) the model equations are written in terms of co-latitude of the place instead of usual latitude, hence the sine and cosine functions of the model equations are modified; and (2) the spherical co-ordinate system used to write the model equations is different from the classical case in the sense that the y-axis (meridional axis) is taken positive towards south and the vertical axis is taken positive in the downward direction. After assuming the approximations of Boussinesq, hydrostatics and the incompressibility of sea water, the final model equations take the following form.

The equations of motion in the zonal (λ), meridional (θ) and vertical (z) directions are respectively of the form

$$\frac{\partial u}{\partial t} + Au + lv + \cot\theta \frac{uv}{R} = -\frac{1}{\rho_0 R \sin\theta}\frac{\partial p}{\partial \lambda} + F^{\lambda}, \tag{1}$$

$$\frac{\partial v}{\partial t} + Av - lu - \cot\theta \frac{u^2}{R} = -\frac{1}{\rho_0 R}\frac{\partial p}{\partial \theta} + F^{\theta}, \tag{2}$$

$$\frac{\partial p}{\partial z} = g\rho. \tag{3}$$

The equation of continuity is expressed as

$$\frac{1}{R\sin\theta}\left[\frac{\partial u}{\partial \lambda} + \frac{\partial(v\sin\theta)}{\partial\theta}\right] + \frac{\partial w}{\partial z} = 0. \tag{4}$$

The equation of state, in which the temperature and salinity are related to the density of sea water, is of the form

$$\rho = \rho(T, S, z). \tag{5}$$

The density of sea water, ρ, is usually written in terms of another variable called sigma-t (σ_t) as $\sigma_t = (\rho - 1)1000$.

The temperature T and salinity S are determined from transport equations of the form

$$\frac{\partial T}{\partial t} + AT = \frac{\partial\left(v_T \dfrac{\partial T}{\partial z}\right)}{\partial z} + \mu_T \Delta T, \tag{6}$$

$$\frac{\partial S}{\partial t} + AS = \frac{\partial\left(v_T \dfrac{\partial S}{\partial z}\right)}{\partial z} + \mu_T \Delta S. \tag{7}$$

In the above equations, θ is the co-latitude, which is equal to $90 - \phi$, with ϕ is the latitude; u, v and w are the velocity components along the east (λ), south (θ) and downward (z) directions respectively; p is the hydrostatic pressure; ρ is the density of sea water, taken as the sum of the constant density, ρ_0, and the density anomaly, ρ'; ρ_0 is the constant density, set equal to 1.0 g cm^{-3}; R is the radius of the Earth; $l = 2\Omega \cos\theta$; Ω is angular velocity of the Earth's rotation; A is the advection operator; Δ is the Laplacian operator; F^λ and F^θ are friction terms in the momentum equations; μ and ν are the horizontal and vertical turbulent viscosity coefficients respectively; μ_T and ν_T are the horizontal and vertical turbulent diffusion coefficients respectively; T is the temperature of sea water; and S is the salinity of sea water.

$$Af = \frac{1}{R \sin\theta}\left(\frac{\partial(uf)}{\partial\lambda} + v\frac{\partial(f\sin\theta)}{\partial\theta}\right) + \frac{\partial(wf)}{\partial z},$$

$$F^\lambda = \frac{\partial\left(\nu \dfrac{\partial u}{\partial z}\right)}{\partial z} + \mu\left(\Delta u - \frac{u}{R^2\sin^2\theta} + \frac{2\cos\theta}{R^2\sin^2\theta}\frac{\partial v}{\partial\lambda}\right),$$

$$F^\theta = \frac{\partial\left(\nu \dfrac{\partial v}{\partial z}\right)}{\partial z} + \mu\left[\Delta v - \frac{v}{R^2\sin^2\theta} + \left(\frac{2\cos\theta}{R^2\sin^2\theta}\right)\frac{\partial u}{\partial\lambda}\right],$$

$$\Delta f = \frac{1}{R^2\sin^2\theta}\frac{\partial^2 f}{\partial\lambda^2} + \frac{1}{R^2\sin\theta}\frac{\partial\left(\sin\theta \dfrac{\partial f}{\partial\theta}\right)}{\partial\theta}.$$

The density of sea water, ρ, is assumed to be the sum of a constant density ρ_0 and a density anomaly $\rho'(\lambda, \theta, z)$. To calculate the pressure gradient terms in Equations (1) and (2) it is necessary to obtain the relation for hydrostatic pressure and the same can be obtained by integrating the hydrostatic equation (3) in the vertical from the free surface to a depth z, i.e.

$$P_z = P_{-\zeta} + g\int_{-\zeta}^{0} \rho \, \mathrm{d}z + g\int_{0}^{z} \rho \, \mathrm{d}z. \tag{8}$$

The following three assumptions were made with regard to the hydrostatic pressure equation (8):

(i) the hydrostatic pressure at the free surface $P_{-\zeta}$ is taken as the surface atmospheric pressure P_a;
(ii) a constant density, ρ_0 (1.0 g cm^{-3}), is used instead of the actual density, ρ, for the calculation of hydrostatic pressure due to the free surface;

(iii) the actual density of sea water below the mean sea level is the sum of a constant density, ρ_0, and a density anomaly $\rho'(\lambda, \theta, z)$.

Taking the above-mentioned assumptions into consideration, the equation for hydrostatic pressure takes the following form:

$$P_z = P_a + g \int_{-\zeta}^{0} \rho_0 \, dz + g \int_0^z (\rho_0 + \rho') \, dz,$$

i.e.

$$P_z = P_a + \rho_0 g\zeta + g\rho_0 z + g \int_0^z \rho' \, dz. \tag{9}$$

The hydrostatic pressure due to a uniform water column of density ρ_0 is normally neglected in baroclinic circulation models. Surface atmospheric pressure P_a is also neglected. The final expression for hydrostatic pressure at depth z is

$$P_z = g\rho_0\zeta + g \int_0^z \rho' \, dz. \tag{10}$$

The density anomaly ρ' and the actual density ρ as defined by Equation (3) are one and the same. The pressure gradient terms in the momentum equations (1) and (2) are to be computed using Equation (10). The unknowns in the model equations are the velocity components (u, v, w), the density anomaly ρ' (actual density), the sea level ζ, the temperature T and the salinity S. It is therefore necessary to derive an additional expression for sea surface topography (sea level) to have a closed system of seven equations in seven unknowns. The detailed procedure of the derivation of the sea surface topography equation is given in Section 4. Considering the assumptions involved in the derivation of hydrostatic pressure, the expression for σ_t is transformed to $\sigma_t = (\rho' - 1)1000$.

2.2. Boundary and initial conditions

The model analysis area lies between the latitudinal belt 30°N–20°S and the longitudinal belt 35°E–80°E (Figure 1). Figure 2 represents a typical box in the finite difference mesh (explained in Appendix A). The entire southern boundary and part of the eastern boundary of the model are open boundaries, where appropriate open boundary conditions for velocity or volume flux are to be specified. The western, northern and part of the eastern boundaries of the model are closed boundaries.

2.2.1. Surface, bottom and lateral (solid) boundary conditions. At the surface ($z = 0$), a rigid lid boundary condition for vertical velocity was employed. Specification of the rigid lid boundary condition at the surface will eliminate short period surface gravitational waves from the solution and will enable us to use larger time steps of integration. However, large-scale waves, such as Rossby and Kelvin waves, are retained in the solution. The wind stress components at the sea surface is related to the velocity components using the gradient transfer hypothesis. For temperature and salinity, the observed values are given. Thus, at the sea surface ($z = 0$), the boundary conditions to be satisfied are

$$W|_{z=0} = 0, \tag{11}$$

$$\rho_0 \nu \frac{\partial u}{\partial z} = -\tau_\lambda, \qquad \rho_0 \nu \frac{\partial v}{\partial z} = -\tau_\theta, \tag{12}$$

$$T|_{z=0} = T^*, \qquad S|_{z=0} = S^*, \tag{13}$$

where τ_λ and τ_θ are the components of wind stress in the zonal and meridional directions respectively, and u and v are the components of velocity fields; T^* and S^* are the observed temperature and salinity data at the surface.

At the ocean bottom, $z = H(\lambda, \theta)$, a non-slip boundary condition for velocity fields was applied, i.e.

$$u = v = w = 0. \tag{14}$$

For temperature and salinity, the following boundary conditions were used:

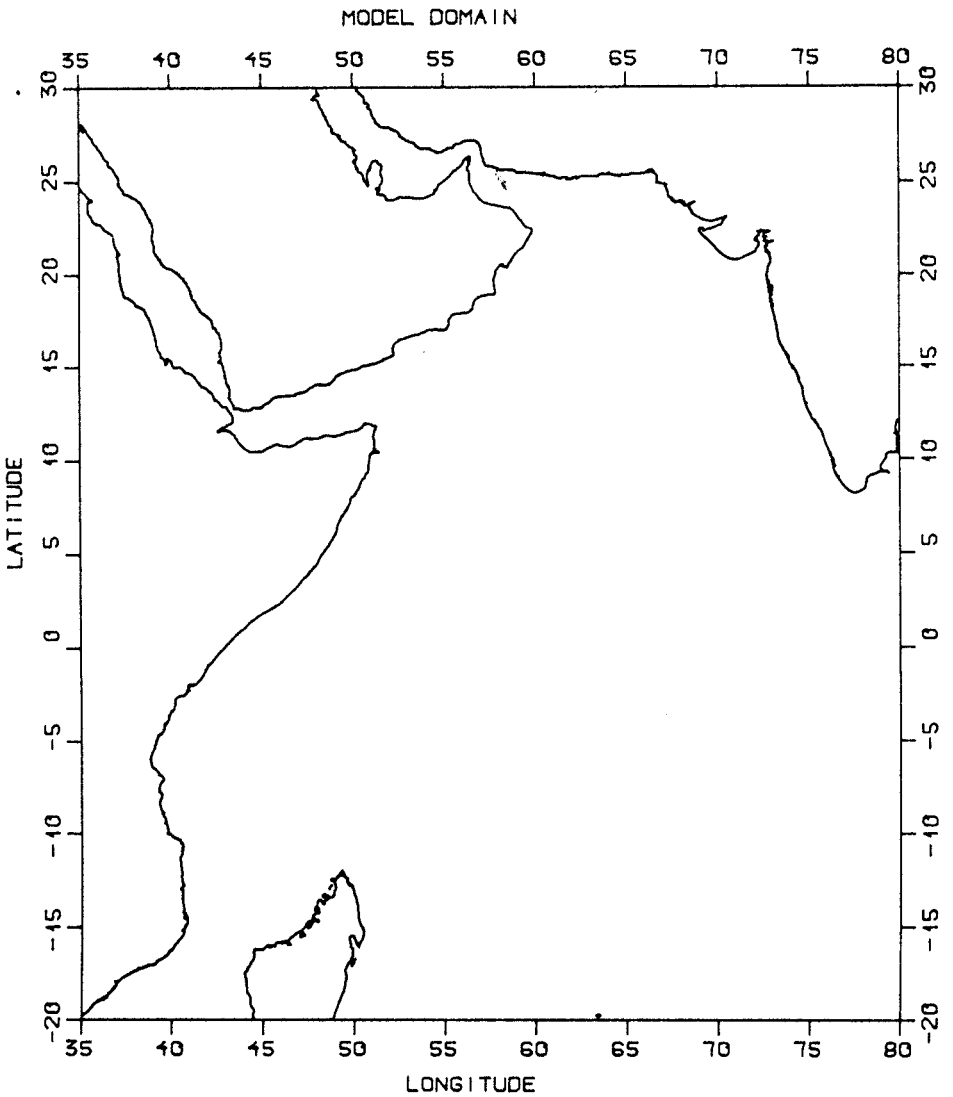

Figure 1. Geometry of the model basin.

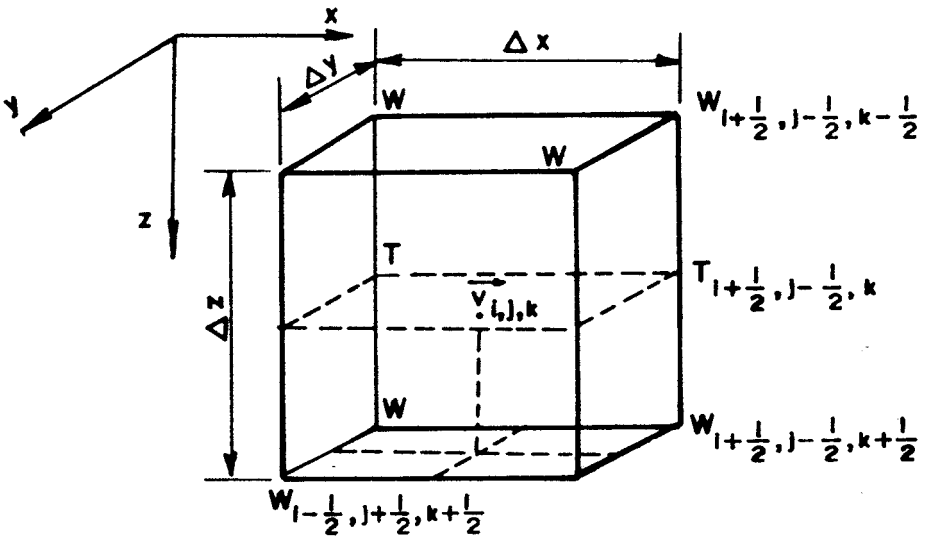

Figure 2. A typical box in the finite difference grid.

$$\frac{\partial T}{\partial \vec{n}} = \frac{\partial S}{\partial \vec{n}} = 0, \tag{15}$$

where $\vec{n}$ is the normal to the sea bottom.

Along the rigid lateral boundaries of the model, the normal flux boundary conditions of zero velocity is prescribed, i.e.

$$\vec{V}_n = 0. \tag{16}$$

For temperature and salinity, we use the following boundary conditions:

$$\frac{\partial T}{\partial \vec{n}} = \frac{\partial S}{\partial \vec{n}} = 0, \tag{17}$$

where $\vec{n}$ is the normal to the lateral boundary.

2.2.2. Open boundary conditions. In order to conserve volume in the model area, the component of velocities or volume flux perpendicular to the open boundary should be balanced. In case the volume flux or the velocities are not balanced, appropriate corrections should be applied to the velocity fields at the boundary so that the velocities are balanced to the maximum extent possible. We have used a quasi-geostrophic model developed by Marchuk and Sarkisyan [9] to compute the velocity components at various levels along the southern and eastern open sea boundaries. This model takes into consideration the wind stress, density field and sea level for the computation of velocity components. The original quasi-geostrophic model of Marchuk and Sarkisyan, written in Cartesian co-ordinates, was converted into a spherical co-ordinate system, since our model equations were written in spherical co-ordinates. The modified quasi-geostrophic formulae for the computation of velocity components are

$$U_{\mathrm{Qg}} = \frac{g}{l}\left[\frac{1}{R}\frac{\partial \eta}{\partial \theta} + \frac{1}{\rho_0 R}\int_0^z \frac{\partial \rho'}{\partial \theta}\,\mathrm{d}z\right] + \frac{\mathrm{e}^{-\alpha z}}{2\rho_0 \alpha \nu}\left[(\tau_\lambda \pm \tau_\theta)\cos \alpha z - (\tau_\lambda \pm \tau_\theta)\sin \alpha z\right], \tag{18}$$

$$V_{\mathrm{Qg}} = -\frac{g}{l}\left[\frac{1}{R\sin\theta}\frac{\partial \eta}{\partial \lambda} + \frac{1}{\rho_0 R \sin\theta}\int_0^z \frac{\partial \rho'}{\partial \lambda}\,\mathrm{d}z\right] + \frac{\mathrm{e}^{-\alpha z}}{2\rho_0 \alpha \nu}\left[(\tau_\theta \pm \tau_\lambda)\cos \alpha z - (\tau_\theta \pm \tau_\lambda)\sin \alpha z\right], \tag{19}$$

where

$$\alpha = \sqrt{\frac{\Omega \sin \Phi}{\nu}},$$

is the Ekman parameter of the ocean. The sea level, η, is computed by means of a dynamic method using the following formula:

$$\eta = \frac{1}{\rho_0} \int_0^H \rho' \, \mathrm{d}z, \tag{20}$$

where H is the reference level. The sign $(+)$ refers to the northern hemisphere. To balance the volume flux or velocity fields across the boundaries, we assume that the volume flux into the model area is positive and that the volume flux out of the model area is negative.

The zonal volume flux across the eastern open sea boundary is calculated using the formula

$$F_{\mathrm{E}} = -\int_{\theta_1}^{\theta_2} \int_0^H U_{\mathrm{Qg}} \, \mathrm{d}z \, \mathrm{d}\theta, \tag{21}$$

where Θ_1 and Θ_2 are the latitudinal extent of the open boundary and H is the depth of the model area.

The meridional volume flux across the southern open boundary is calculated using the formula

$$F_{\mathrm{S}} = -\int_{\lambda_1}^{\lambda_2} \int_0^H V_{\mathrm{Qg}} \sin \theta \, \mathrm{d}z \, \mathrm{d}\lambda, \tag{22}$$

where λ_1 and λ_2 are the longitudinal extent of the zonal open boundary.

The total volume flux ($F_{\mathrm{T}} = F_{\mathrm{E}} + F_{\mathrm{S}}$) across the eastern and southern boundaries must be balanced to conserve volume in the model area. If the total volume flux across the southern and eastern boundaries are not balanced, we must apply a velocity correction to all the grid points in the open boundaries, taking into consideration the total volume flux (residual volume of water). It has been found that while there was an approximate balance between the incoming and outgoing volume fluxes across the southern open sea boundary, these were not balanced across the eastern boundary because of the massive zonal fluxes into the model area from the system of zonal currents in the equatorial currents. In view of this, we applied a velocity correction at all the grid points in the open boundaries. The velocity correction, V_{c}, to every point in the open boundary, considering the total flux, can be written as

$$V_{\mathrm{c}} = \frac{F_{\mathrm{T}}}{A}, \tag{23}$$

where A is the total lateral surface area of the open boundary. This velocity correction was added to the quasi-geostrophic velocities computed by formulae (18) and (19).

For the eastern open boundary, the corrected u component of the quasi-geostrophic velocity is

$$U_{\mathrm{Qg}} = U_{\mathrm{Qg}} + V_{\mathrm{c}}. \tag{24}$$

For the southern open boundary, the corrected v component of the quasi-geostrophic velocity is

$$V_{\mathrm{Qg}} = V_{\mathrm{Qg}} + V_{\mathrm{c}}. \tag{25}$$

After having corrected the velocities at each grid point, the balance of the normal component of the quasi-geostrophic velocities (Equations (18) and (19)) were again calculated for the conservation of volume. In our model, a velocity balance of 0.002 cm s^{-1} was achieved across the open sea boundaries.

The v component of the quasi-geostrophic velocity as computed by Equation (19) and the corrected zonal component of velocity as calculated by Equation (24) were prescribed at the eastern open boundary. At the southern open sea boundary, the u component of the quasi-geostrophic velocity as computed by Equation (18) and the corrected meridional component of velocity as calculated by Equation (25) were prescribed. The prescribed velocity components were kept constant throughout the model integration.

The temperature and salinity at the open sea boundaries were given as follows:

$$T|_L = T^*, \qquad S|_L = S^*, \tag{26}$$

where T^* and S^* are the observed temperature and salinity data.

2.2.3. Initial conditions. The model integration starts with an initial state of rest for the velocity fields and for temperature and salinity, the observed values are specified at time $t = 0$,

$$(u, v)_{t=0} = 0,$$

$$(T, S)_{t=0} = (T^*, S^*).$$

The finite difference formulation of the governing equations is given in Appendix A. The derivation of the sea surface topography equation based on the solutions of the finite difference equations of momentum, hydrostatics and continuity is also given in Appendix A.

3. NUMERICAL SOLUTION PROCEDURE

The semi-diagnostic model consists of a total of seven equations in seven unknowns; these equations are the prognostic equations of horizontal velocity fields, temperature and salinity and diagnostic equations, such as the equation of continuity, the sea level equation and the equation of state. The unknowns are the velocity components (u, v, w), the density anomaly (actual density), the temperature, the salinity and the sea surface topography.

Hydrodynamical adjustment is carried out in two stages: during the first stage, which is called the diagnostic stage, the model equations of momentum, hydrostatics, continuity and sea surface topography were solved with appropriate boundary and initial conditions given in the previous sections. The equation of state is used to compute the density field and the latter is kept constant throughout the first stage of model integration. The model is integrated for approximately 1 month, by which time the flow fields are generated completely. During the second stage, which is called the adaptation stage, the full set of seven equations that include the turbulent diffusion equations of heat and salt were again integrated for approximately 1 month, with the initial conditions for flow fields obtained from the first diagnostic stage. The initial conditions for temperature and salinity during the adaptation stage are the original temperature and salinity data which were used for the diagnostic calculations. During the adaptation stage, the input of density field was smoothed and the flow fields and other hydrological variables were hydrodynamically adjusted with wind field and bottom topography. We used the adjustment criteria developed by Marchuk and Sarkisyan [9] to decide about the maximum time of integration of the model. The adjustment test is

$$\xi = \min \Phi(t),$$

where

$$\Phi(t) = \frac{f^{n+1} - f^n}{\sqrt{\left(\frac{\partial f}{\partial x}\right)^2 + \left(\frac{\partial f}{\partial y}\right)^2}}. \tag{27}$$

In Equation (27), f is any of the hydrological parameters, such as temperature, salinity or density field, and n is the number of time steps. The criterion is based on the assumption that during the first stage of integration, i.e. the adaptation stage, the numerator of (27) decreases much faster than the denominator (horizontal gradient of properties). At the second stage, the numerator does not decrease so rapidly. Its decrease becomes almost the same as that of the denominator. This means that some optimum stage is reached when hydrological fields were adjusted hydrodynamically and the property gradients were not smoothed by dissipative forces. If the model integration is continued for a long time, the property gradients will be greatly smoothed and the hydrological fields (temperature and salinity) will be greatly deviated from the original temperature and salinity data. In our model, the total integration time for both the diagnostic and adaptation stages is approximately 2 months.

4. NUMERICAL EXPERIMENTS

4.1. Introduction

Two types of numerical experiments are described. First, the 18-level adaptation model with a flat bottom at 900 m is used to investigate the sensitivity of the solution to different eddy viscosity and diffusivity coefficients. Altogether, three numerical experiments were conducted for the month of February to select the appropriate coefficients for the calculation of climatological mean circulation. In the second experiment, the 33-level adaptation model is used for the computation of seasonal mean climatological circulation during Spring. The model is driven by the wind stress forcing at the sea surface and by thermohaline forcing at different model levels. The horizontal dimension of the model is 1° in the zonal and meridional directions, and standard oceanographic depths are chosen in the vertical direction, with the time increment Δt being 1 h.

4.2. Experiment 1: sensitivity experiments

Generally, in large-scale ocean circulation models, the eddy coefficients through which fluxes of momentum, heat and salt are represented are parameterised either in terms of known measurable variables or with constant values. Values of these eddy coefficients vary widely in space and time; e.g. while the horizontal eddy viscosity and diffusivity coefficients vary from 10^6 to 10^{10} $cm^2\,s^{-1}$, the vertical eddy viscosity and diffusivity coefficients vary from 10^{-1} to 10^3 $cm^2\,s^{-1}$. It assumes different values at different seasons for the same location. Reasonable values of these coefficients can be obtained by making microstructure measurements of physical oceanographic variables, such as currents, temperature and salinity, at different environmental conditions at different places and then compute the values of these coefficients through appropriate empirical and semi-empirical formulae. Such empirically determined values could be used in numerical models to obtain a reasonable picture of ocean circulation. Until now, there has not been any such measurements for the computation of eddy coefficients in the Indian Ocean area.

Woods [12] suggested that prognostic ocean circulation models capable of predicting climate on a decadal time scale should have realistic parameterisations of these coefficients; however, it is not essential to parameterise these coefficients in diagnostic and semi-diagnostic models of circulation that are intended for the computation of climatological mean circulation in the ocean. We can use constant values of these coefficients in such models and appropriate constant values can be obtained through numerical experiments.

In this study, we have used the monthly mean wind data compiled by Hellerman and Rosenstein [13], and the temperature and salinity data is obtained from *The Climatological Atlas of the World Oceans* by Levitus [14]. To study the sensitivity of the solution to different eddy coefficients, the 18-level semi-diagnostic model of circulation was driven with February's mean data on wind field and temperature, and Winter's mean data on salinity, which corresponds to February's salinity distribution. It has become necessary to use Winter mean salinity data for the calculation of circulation during February since mean salinity data for February on a 1° space scale were not available for our model area. It is reasonable to assume that there is no significant variability in the salinity distribution from month to month within a particular season.

4.2.1. Model forcing parameters. The spatial distribution of monthly mean resultant wind stress for February is given in Figure 3. During February, the northeast monsoon winds blow northeasterly and easterly over the entire Arabian Sea north of equator. The maximum stress reaches up to 1 dyne cm^{-2} off the Somali and African coasts. The strength of the northeasterly winds is reduced on crossing the equator and it becomes very weak on reaching the East African coast. Calm winds prevail in the doldrums region. Southeasterly winds with magnitudes greater than 1 dyne cm^{-2} are observed in the southern hemisphere between 13°S and 20°S. The wind is westerly in the belt between 5°S and 13°S and longitude east of 45°E.

Apart from wind stress forcing, the density fields at various levels for February are also computed to drive the model. As mentioned earlier, February mean temperature data and Winter mean salinity data were used to calculate the σ_t for February. Figure 4(a) and (b) depicts the σ_t at 10 and 150 m respectively for February. At 10 m, high dense water is found in the northern and central Arabian Sea, with σ_t attaining a value of 24.8 in the northern Arabian Sea. The presence of high dense waters in this region is attributed to the excess of evaporation over precipitation. The density decreases towards the equatorial regions and low dense waters, with a σ_t of 22.2, are observed in the central equatorial Indian Ocean. Density is further reduced off the southwest coast of India due to the presence of low-saline Bay of Bengal waters advected to this region.

At 150 m (Figure 4(b)), high dense waters are observed in the central Arabian Sea, Arabian and African coasts and in the equatorial regions, where σ_t attains a value as high as 25.8.

Table I shows the details of parameter values used in all the three sensitivity experiments.

4.2.2. First sensitivity experiment. In the first sensitivity experiment, the lateral friction and diffusivity coefficients were kept at a low value of 5×10^7 $cm^2\,s^{-1}$. The vertical turbulent diffusion coefficient is also kept at a low value of 1 $cm^2\,s^{-1}$. The vertical turbulent mixing coefficient is kept at a constant value of 10 $cm^2\,s^{-1}$ for all the numerical experiments.

Figure 5(a) and (b) show the computed current at 10 and 150 m respectively for the first experiment. The flow field north of the equator is southwestward and southward in response to the northeasterly and northerly winds. The computed currents in this region more or less follow the wind pattern. Analysis of the density field at 10 m (Figure 4(a)) show that the isopycnal surfaces are oriented in a northeasterly–southwesterly direction and there is a gradual decrease in density from the north to the south. Such a density structure would

generate a weak geostrophic flow towards southwest. The northeast monsoon current found north of the equator is the resultant of both the wind stress and thermohaline forcing. The southwestward flow along the Somali and African coasts attain speed as high as 1 m s^{-1} during February. The westward and northwestward flowing South Equatorial Current (SEC), located between 10°S and 20°S, is generated by the prevailing SE trades. At the east coast of Madagascar, a weak southward-flowing East Madagascar Current (EMC), which is fed by the SEC, is observed. With the further extension of the SEC, there is a broad southward flowing western boundary current, namely the Mozambique Current (MZC). The eastward-flowing Equatorial Counter Current (ECC) is located between 3°S and 10°S and the same is fed partly by the SEC and the southward-flowing northeast monsoon current at its western origin. The westerly winds in this region make this flow more zonally oriented.

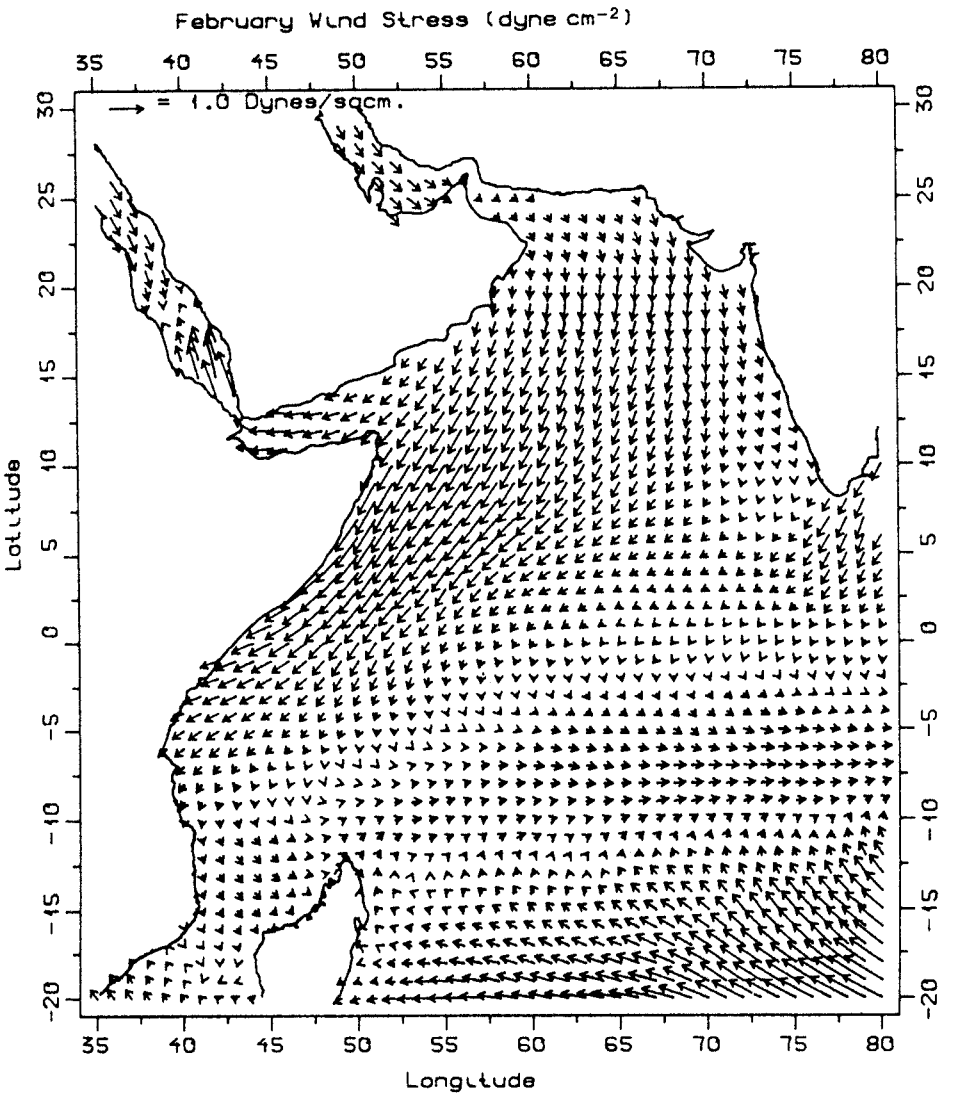

Figure 3. Spatial distribution of February mean resultant wind stress (dyne cm^{-2}).

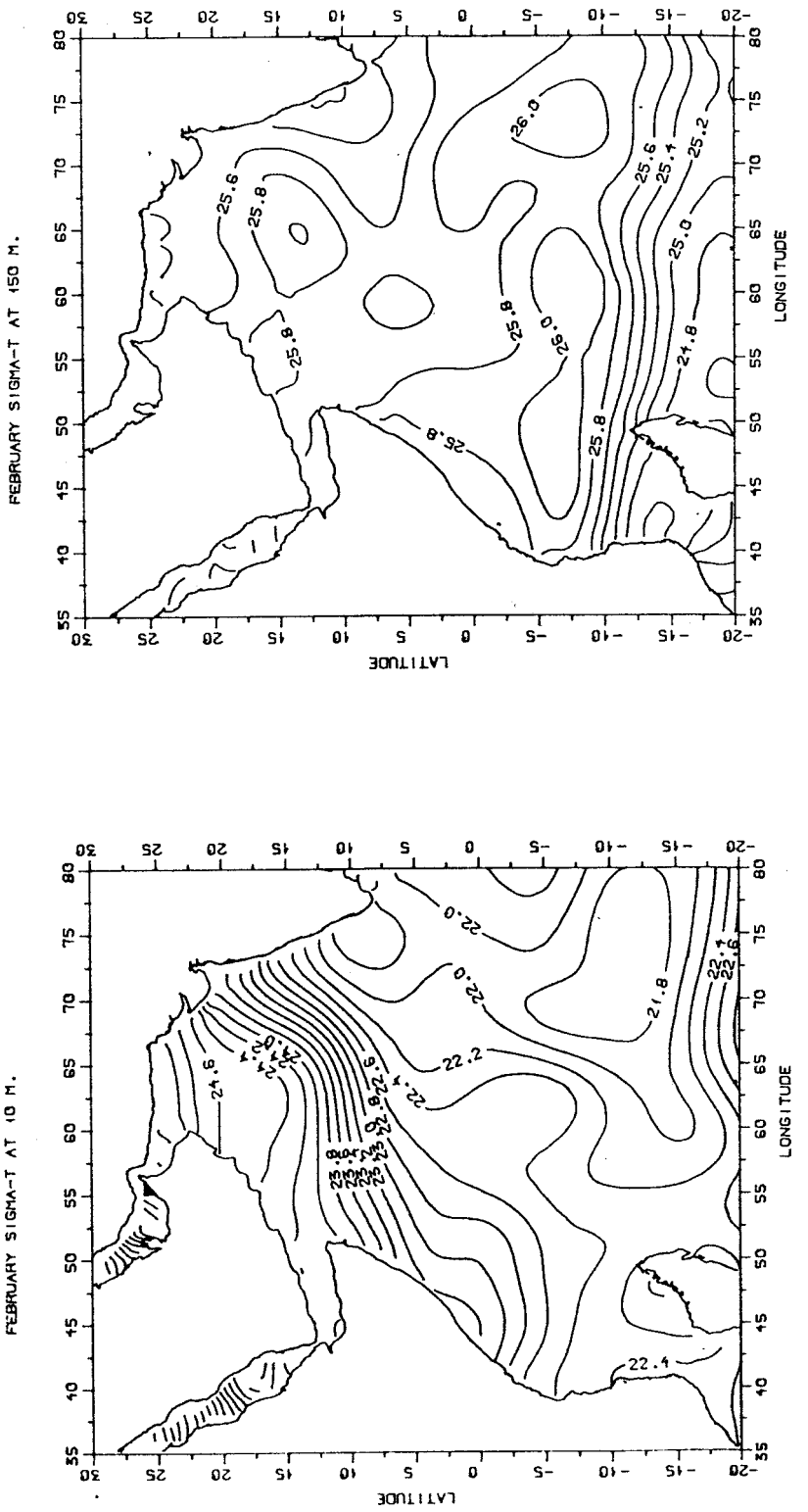

Figure 4. Spatial distribution of σ_t during February at (a) 10 m and (b) 150 m.

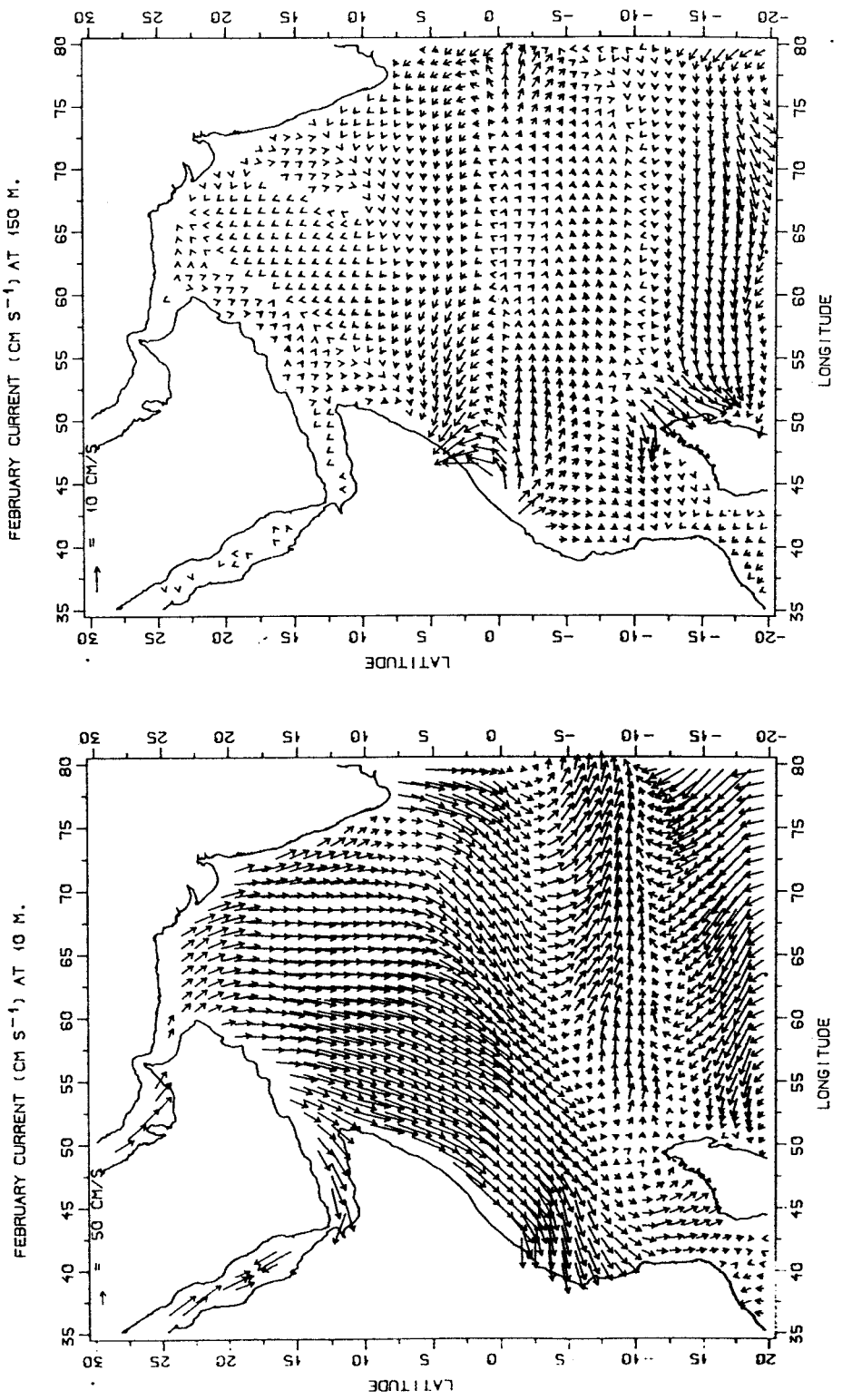

Figure 5. Computed February mean current at (a) 10 m and (b) 150 m for the first sensitivity experiment.

Table I. Summary of parameter values used in the sensitivity experiments.

Sl. number	Name of the parameter	Notation	Parameter values used		
			Experiment 1	Experiment 2	Experiment 3
1	Horizontal turbulent mixing coefficient	μ	5×10^7	10^8	5×10^8
2	Vertical turbulent mixing coefficient	ν	10	10	10
3	Horizontal turbulent diffusion coefficient	μ_t	5×10^7	10^8	5×10^8
4	Vertical turbulent diffusion coefficient	ν_t	1	5	10

The computed currents at 10 m (Figure 5(a)) can be compared with ship drift measurements of surface currents, compiled by Cutler and Swallow [15]. The original ship drift climatology was interpolated using a cubic spline to $1^\circ \times 1^\circ$ resolution for a better comparison with the model results. Figure 6 depicts the ship drift current for February in the model area. A comparison of Figures 5(a) and 6 shows that the model reproduced the currents in the southern tropical Indian Ocean (between 10°S and 20°S), such as the SEC, the MZC, the EMC in their respective locations. Ship drift measurements show the northward-flowing East African Coastal Current (EACC), whereas the model did not reproduce the same. The computed currents along other parts of African coasts are in good agreement in terms of magnitude and direction with ship drift measurements. The observed ECC is limited to a narrow belt between the equator and 5°S as compared with the model computed ECC located between 3°S and 10°S. The observed currents north of the equator are more or less southwestward, which is in good agreement with the model results.

The computed current at 150 m (Figure 5(b)) is entirely different from what is observed at the surface and this difference in the circulation features can be explained in terms of the distribution of σ_t and sea surface topography. We shall first describe the variability of circulation and sea surface topography and the dynamics of steady state circulation in terms of the local forcings of density, wind field and sea level will be explained in the subsequent paragraphs.

Between 10°S and 20°S, the westward-flowing SEC is present throughout the entire breadth of the model area, stretching from 35°E to 80°E. The magnitude of this current is of the order of 10–15 cm s^{-1}. The northern branch of the SEC on reaching the east coast of Madagascar turns southwards and flows as a coastal under current. A part of the northern branch of the SEC on reaching the East African coast turns eastward and flows as the Equatorial Under Current (EUC). During the northeast monsoon season, a strong EUC is located in the thermocline region and our model results also show the presence of eastward-flowing EUC between the equator and 10°S. The presence of the EUC is reflected in the sea surface topography distribution, which forms a closed clockwise loop between the equator and 20°S (Figure 7). The zonal sea level gradient that exists between the East African coast and offshore regions is responsible for the generation of the EUC. Between the equator and 10°N, the westward-flowing North Equatorial Current (NEC) is still observed at 150 m with comparatively less magnitude. One branch of the NEC south of the Indian Peninsula flows northwest along the southwest coast of India as a coastal under current and this northward flow is located up to the central west coast of India. A weak clockwise gyre-type of circulation is

formed in the northern Arabian Sea covering the coastal regions of Arabia and the northwestern coastal regions of India. Along the coastal regions of northern Somalia, a southward-flowing subsurface current is observed in the model results and its presence has been reported by Quadfasel and Schott [16] who deployed moored current meters off Somalia near 5°N.

Figure 7 depicts the distribution of sea surface topography computed by the model. Sea surface topography is mainly controlled by the wind field at the sea surface level, density variations in the vertical and the flow field in the interior of the ocean especially in the thermocline region. In fact, the thermocline circulation is mainly controlled by the sea surface topography distribution as the wind effects are negligible at this depth. Features such as gross thermocline shape, powerful surface boundary currents and strong tropical circulation patterns

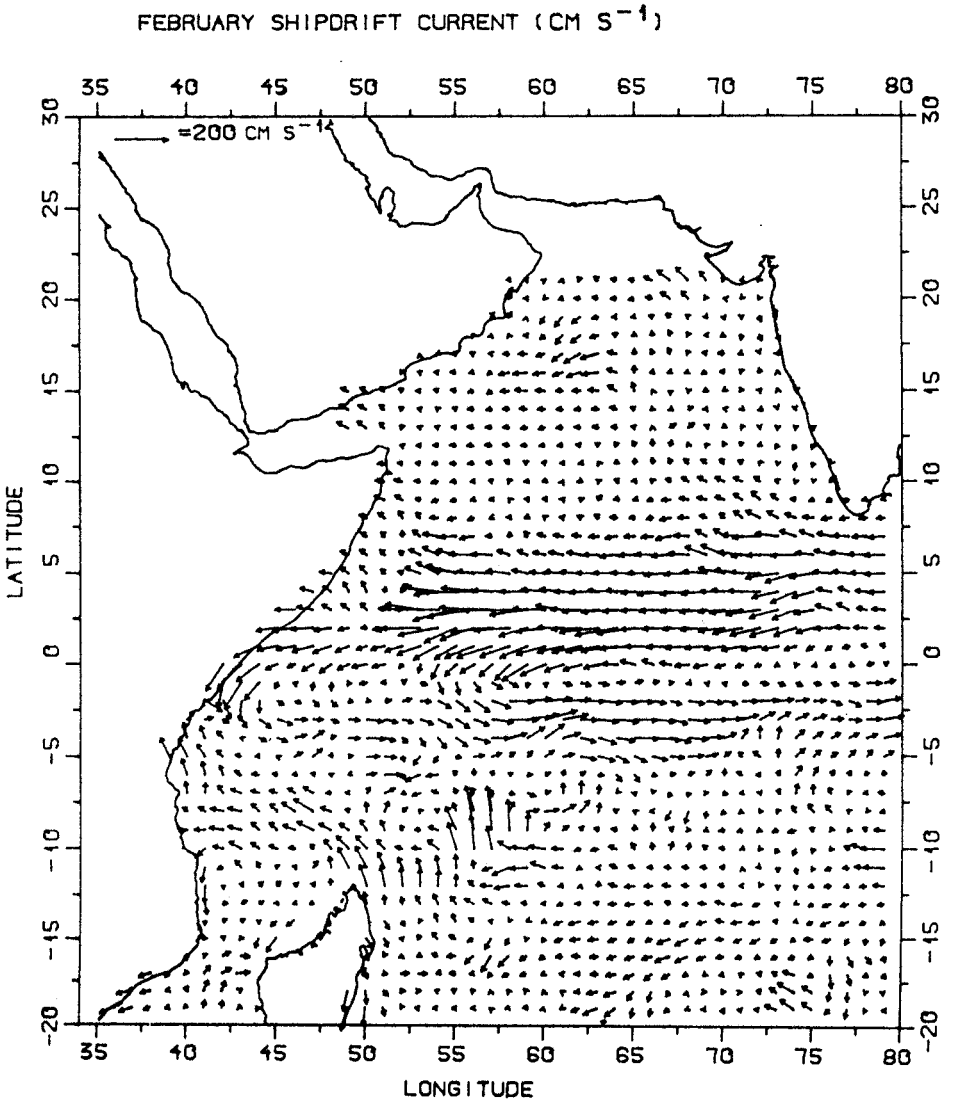

Figure 6. The ship drift surface current of Cutler and Swallow [15] for February.

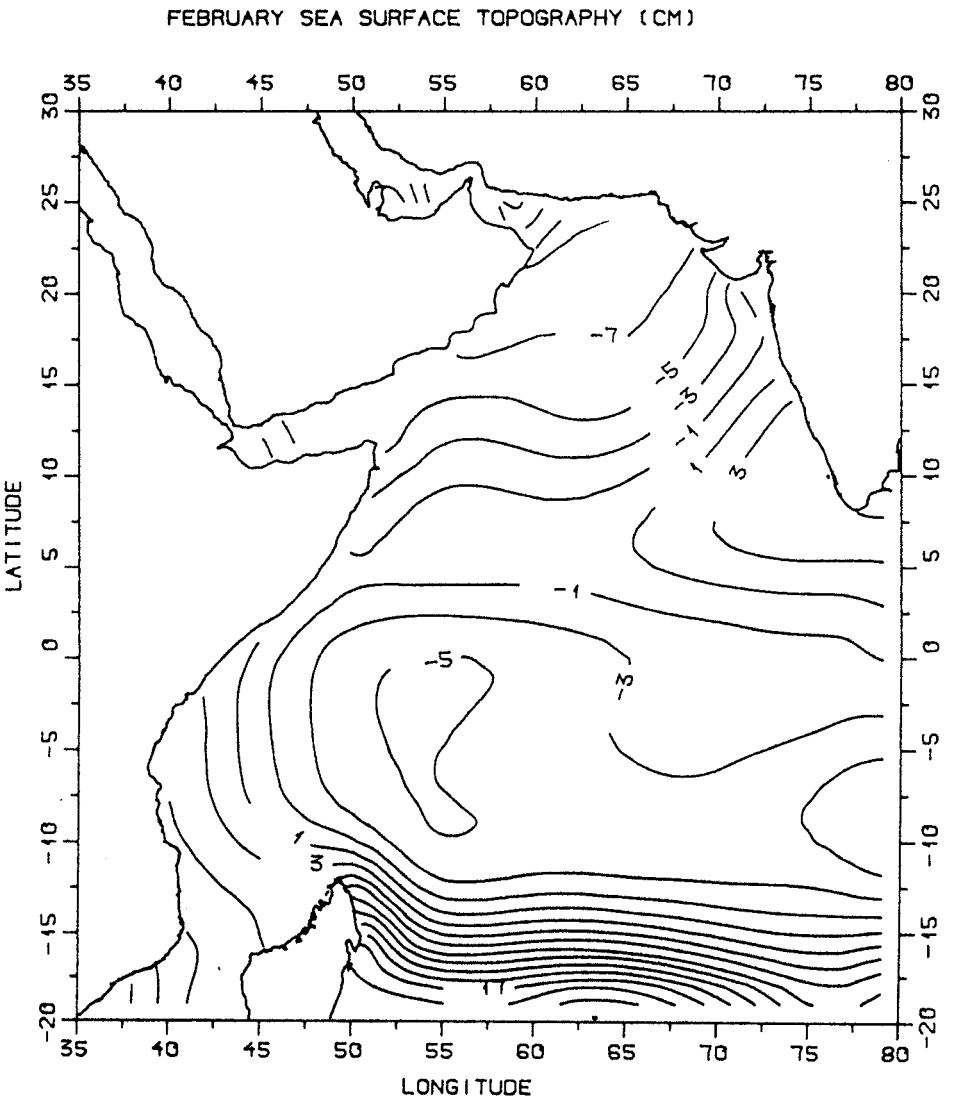

Figure 7. Computed sea surface topography (cm) for February during the first sensitivity experiment.

are all reflected in the sea surface topography. In the southern hemisphere between 10°S and 20°S, a zonally oriented ridge with a steep downward slope towards the equator is observed along the entire stretch of the model area, between 35°E and 80°E. The sea level gradually decreases from the southern tip of India to the northern Arabian Sea in a northwesterly direction, and the difference in sea level between the equator and northern most part of Arabian Sea is found to be of the order of 16 cm. The difference in sea level in the SEC region is approximately 28 cm, and such large differences in sea level at this region can be attributed to the sharp variation in the density field and the Ekman wind drift, which is directed to the left of the wind direction in the southern hemisphere. There is a strong hydrochemical front at 10°S and this front is more pronounced in the subsurface layers than at the surface. Maps of salinity at all the horizons between 100 and 500 m show that there is a distinct horizontal

salinity minimum stretching along 10°S all the way from Timor to the north of Madagascar. This minimum in salinity is caused by the advection of low salinity waters by the SEC from the Timor Sea and the waters between Australia and Indonesia, as reported by Wyrtki [17].

A close examination of sea surface topography distribution of σ_t surfaces and computed current at 150 m shows that the SEC located south of 10°S is mainly forced by the sea surface topography. The westward-flowing SEC at 150 m is essentially a geostrophic current caused by the balance of Coriolis force and the north–south pressure gradient that exists between 10°S and 20°S. Both the density variation and sea surface topography drive the northward coastal under current observed along the southwest coast of India during Winter.

4.2.3. Second sensitivity experiment. In the second sensitivity experiment, the horizontal eddy viscosity and the diffusivity coefficients were increased twofold and the vertical eddy diffusivity was increased by fivefold to study the combined effects of these parameters on circulation and sea surface topography (Table I).

The circulation pattern did not change much at 10 m with these coefficients (Figure 8(a)) except that the magnitude of current vectors were decreased by 1–3 cm s^{-1} in those regions where the horizontal shear was found to be more. This marginal decrease in the intensity of currents can be attributed to the use of higher lateral friction and diffusivity coefficients.

At 150 m, a noticeable change can be observed in terms of magnitude and direction of currents in the model area (Figure 8(b)). The EUC is well reproduced in this experiment with its intensity reduced by 3–4 cm s^{-1}. The currents along the coasts of Africa and Madagascar regions became smooth because of the use of high horizontal and vertical eddy diffusivity coefficients. The anticlockwise eddy found off the coast of Africa is also well smoothed in this experiment. This experiment shows that the vertical diffusivity coefficient is an important parameter for the horizontal distribution of currents in the thermocline regions.

Figure 9 shows the computed sea surface topography for the second numerical experiment. A comparison of Figures 9 and 7 shows that there is no appreciable change in the magnitude of sea surface topography in both these experiments. The sea level contours are more smoothed off the African coast in the second experiment.

4.2.4. Third sensitivity experiment. In the third experiment, the values of horizontal eddy coefficients were increased fivefold as compared with the second experiment. The vertical friction and diffusion coefficients were given the same value of 10 $cm^2\ s^{-1}$. Figures 10 and 11 show the computed current and sea surface topography respectively of the third experiment. In this experiment, a perceptible change is observed in the circulation pattern at 150 m (Figure 10(b)). However, not much change in circulation is observed at 10 m as compared with the previous experiment. The southward-flowing Somali subsurface current, eastward equatorial undercurrent and the westward flow between 10°S and 20°S were reproduced well in this experiment. This experiment shows that the vertical friction and diffusion coefficient should be given the same values to reproduce realistically the currents in the thermocline regions. The value of the sea level is reduced marginally in the central Arabian Sea.

During the three sensitivity experiments mentioned above, the values of lateral friction coefficients were varied from 5×10^7 to 5×10^8 $cm^2\ s^{-1}$. The main objective of all these experiments was to select the most appropriate coefficients, both horizontal and vertical, to calculate the climatic circulation in the Arabian Sea. To compare the differences in the magnitude of currents between these numerical experiments, we have plotted the magnitude of the resultant current at 10 and 50 m along the equator (Figure 12). It is found that the differences in magnitude between different numerical experiments are negligible at 10 m; however, a difference of 5–7 cm s^{-1} in intensity was noted at 50 m between the first and

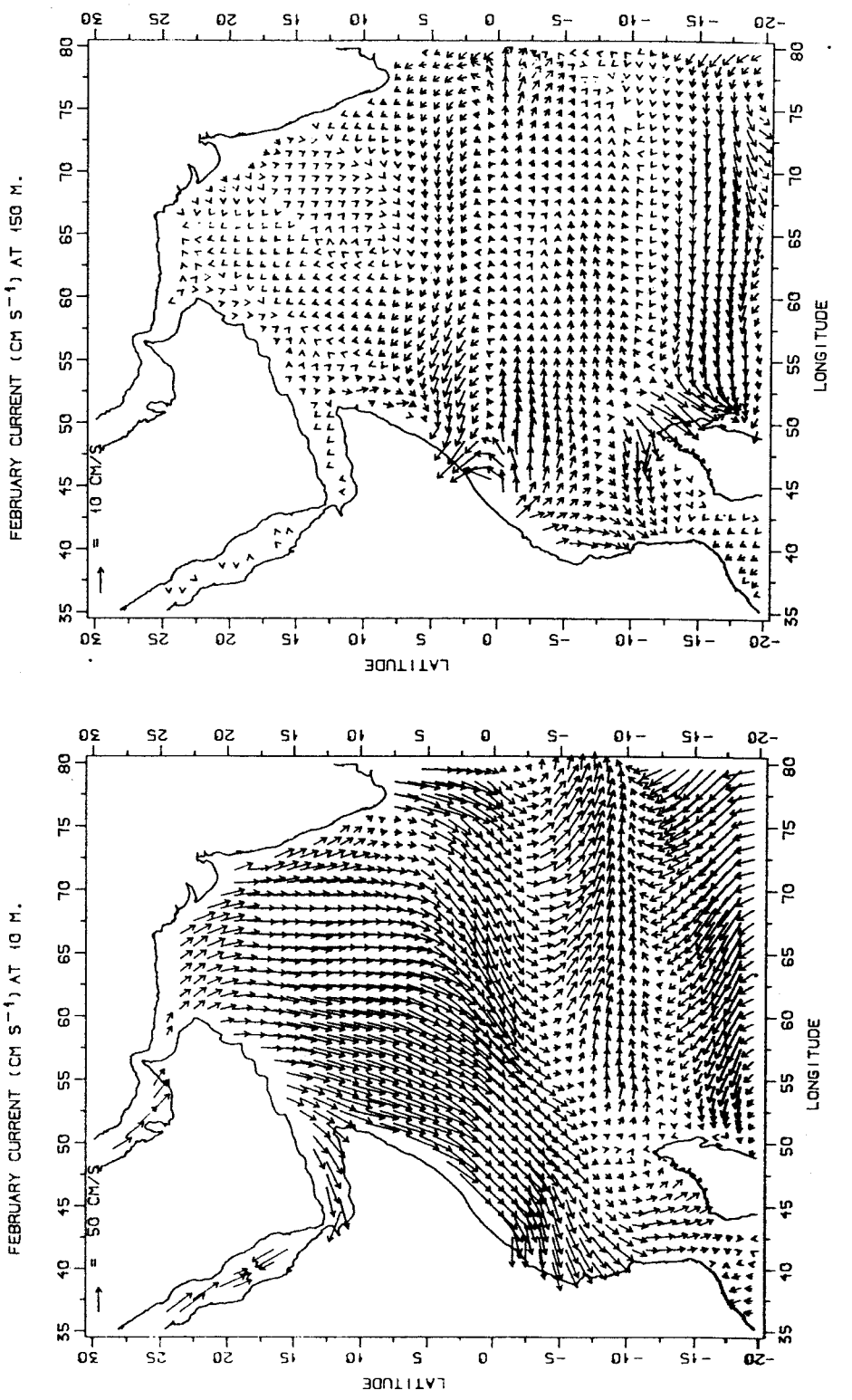

Figure 8. Computed February mean current at (a) 10 m and (b) 150 m for the second sensitivity experiment.

second experiments because of the twofold increase in the horizontal mixing coefficient. The non-linear terms play a significant role in the equatorial regions where the Coriolis effect is less as compared with off-equatorial regions. When the magnitudes of horizontal exchange terms exceed the magnitudes of non-linear terms by one order, the magnitudes of the later would be relatively low. At higher values of horizontal exchange coefficients, there will not be much intensification of currents and the same is more noticed in the equatorial regions. From the above three numerical experiments, it is concluded that the values of coefficients used in the third experiment are the most appropriate ones for the calculation of seasonal and monthly mean climatic circulation in the Arabian Sea.

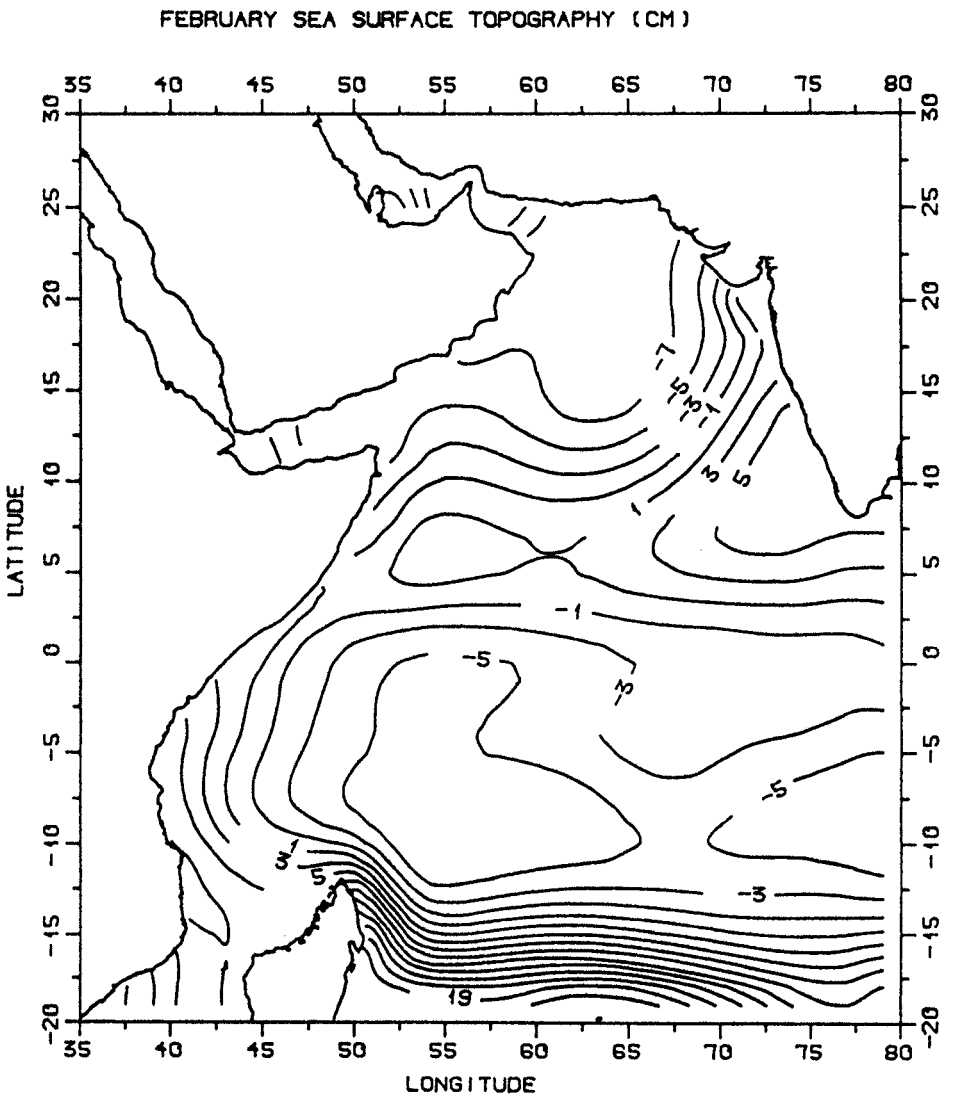

Figure 9. Computed sea surface topography (cm) for February during the second sensitivity experiment.

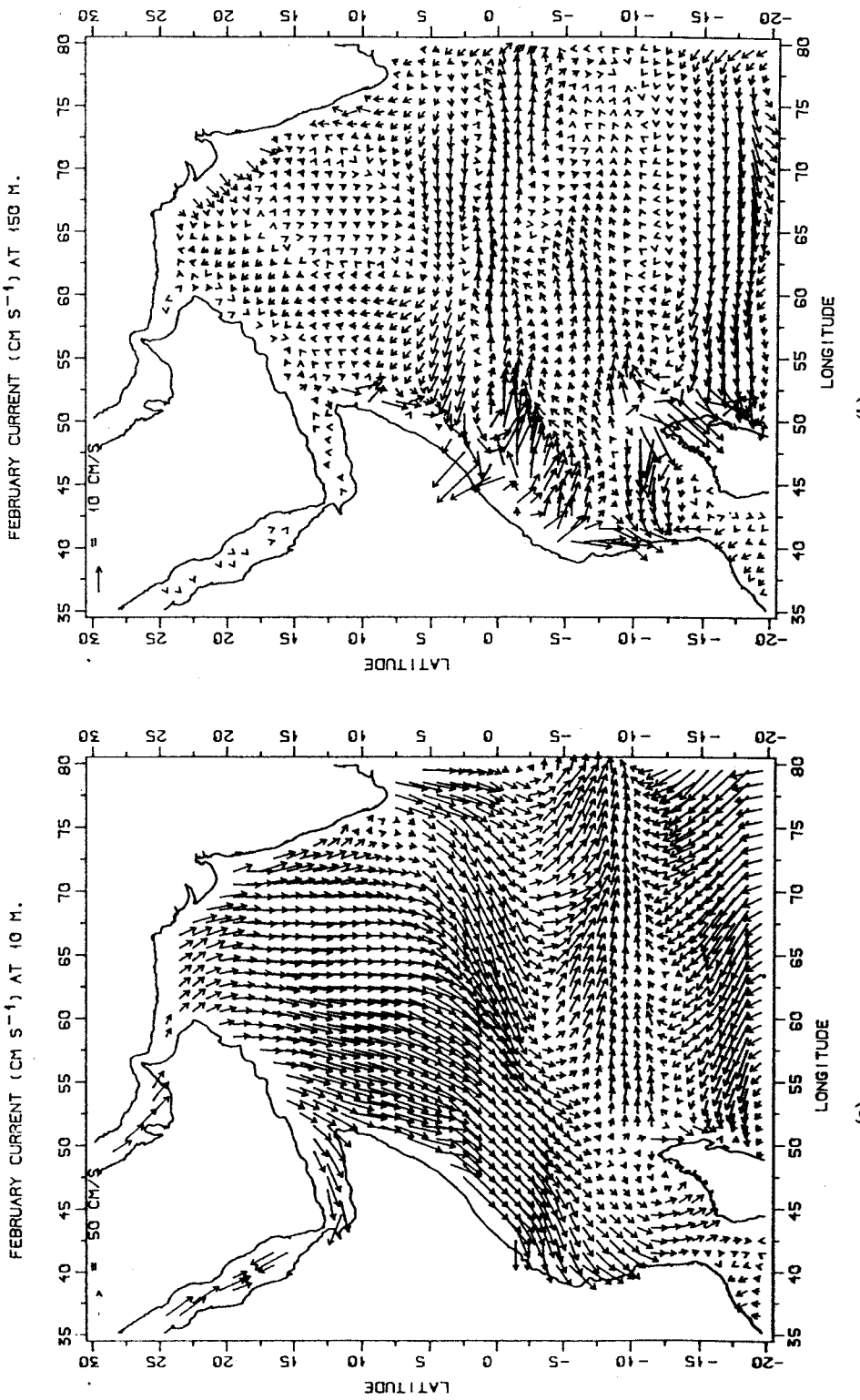

Figure 10. Computed February mean current at (a) 10 m and (b) 150 m for the third sensitivity experiment.

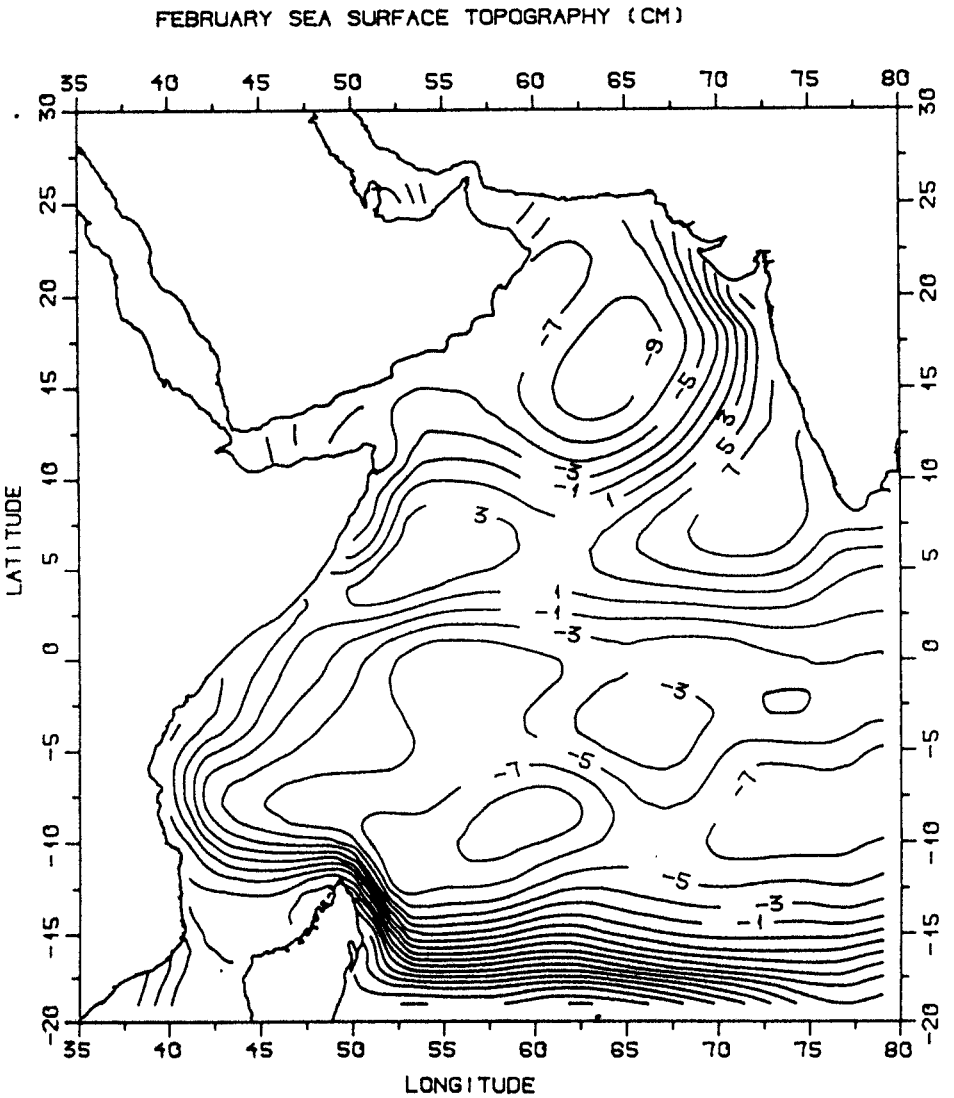

Figure 11. Computed sea surface topography (cm) for February during the third sensitivity experiment.

4.3. Experiment 2: climatological circulation for the spring season

In this experiment, the 33-level adaptation model is used for the computation of climatological seasonal mean circulation for Spring. The climatological seasonal mean wind data for Spring required to drive the model are obtained from the wind field compiled by Hellerman and Rosenstein [13]; the internal density field at various levels necessary to initialise the model is obtained from the climatology data of Levitus [14] on temperature and salinity. The adapted (steady state) results of currents, sea surface topography, temperature and salinity anomaly fields are presented.

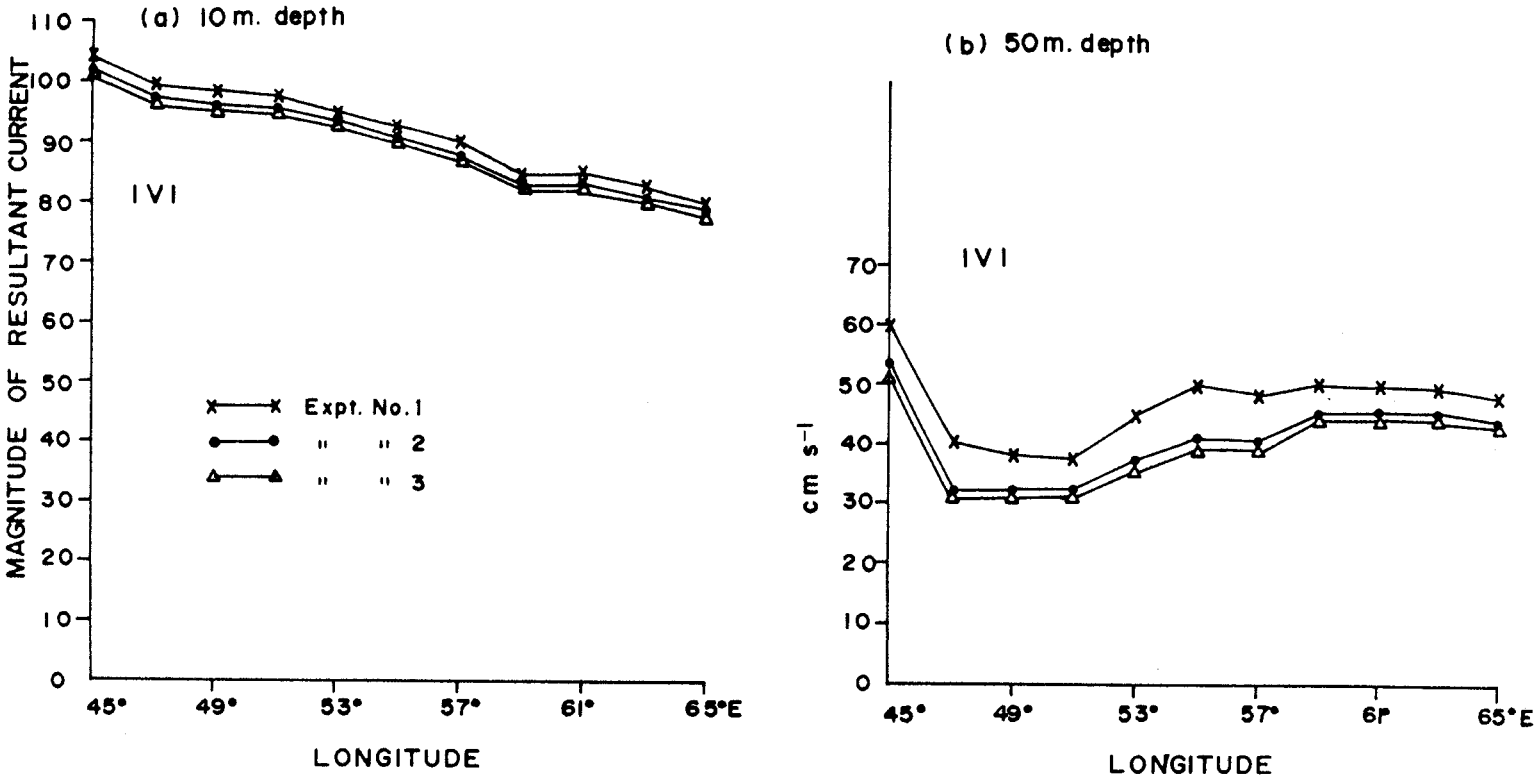

Figure 12. Intensity of resultant current $|\vec{V}|$ at (a) 10 m and (b) 50 m along the equator for different numerical experiments.

4.3.1. Model forcing parameters. Brief descriptions of the forcing parameters, such as wind field at the sea surface level and density (σ_t) at selected levels (six levels), are given before presenting the results on currents and sea surface topography. The spring mean wind stress (dyne cm^{-2}) for the model area that lies between 30°N and 20°S and 35°E and 80°E is presented in Figure 13. Strong southeasterly winds with magnitudes greater than 1 dyne cm^{-2} are observed during Spring in the southern hemisphere between 10°S and 20°S. The winds turn southerly on approaching the equator and then turn southwesterly after crossing the equator. Westerly winds prevail in the equatorial belt of the central Arabian Sea between 5°N and the equator. Southwesterly winds with magnitudes greater than 1.5 dyne cm^{-2} are observed off the Somali coast and in the northern Arabian Sea.

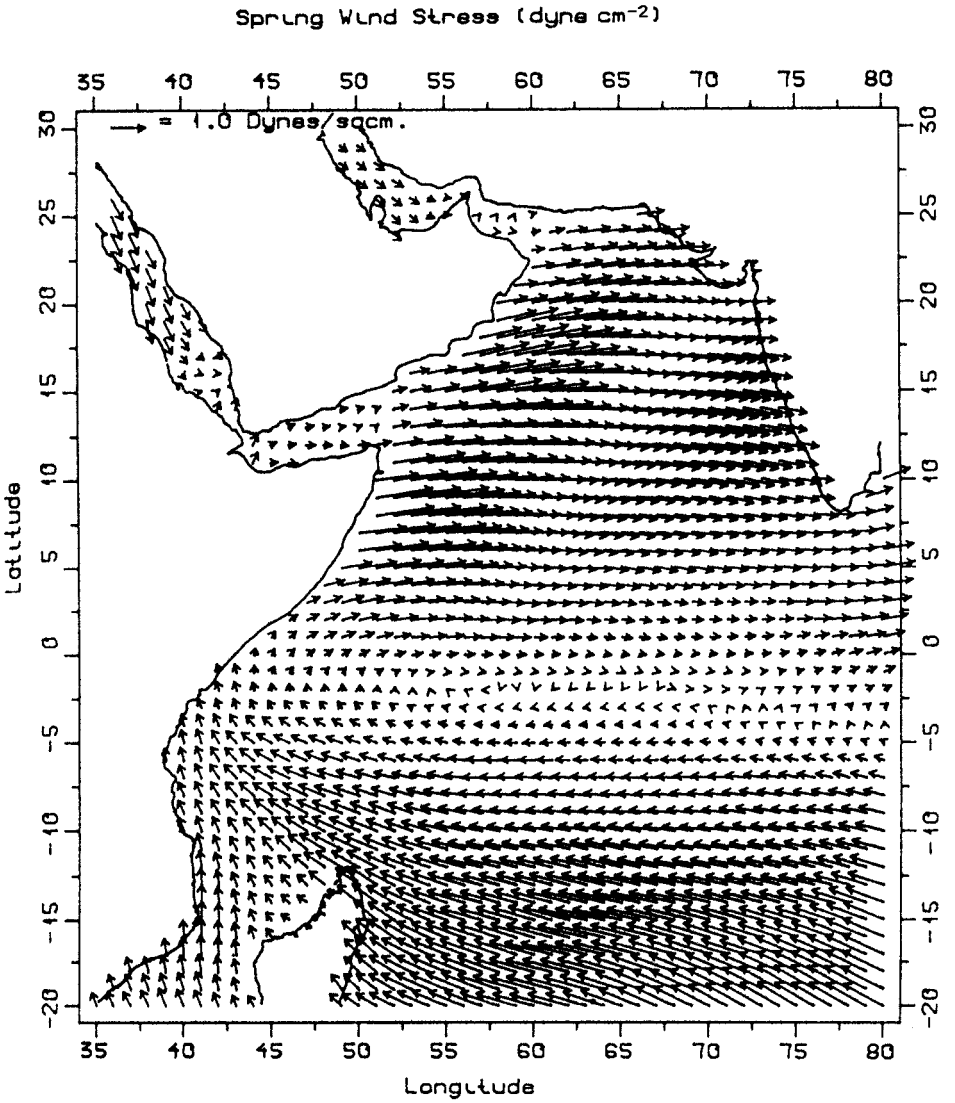

Figure 13. Spatial distribution of mean resultant wind stress (dyne cm^{-2}) during Spring.

The mean σ_t field during Spring at 20, 50, 150, 300, 500 and 1000 m are presented in Figure 14(a)–(f). At 20 m, between 20°S and the equator, the σ_t values vary from 23.6 at 20°S to approximately 22.0 near the equator. Off the Somalia and Arabian coasts, σ_t values are fairly high due to the presence of high dense water. At 50 m, high dense water with a σ_t value of 24.0 is observed at the southwestern sector of the model domain. There is an increase in density in the northern extremity of the Arabian Sea when compared with its distribution at 20 m.

At 150 m (Figure 14(c)), significant changes in σ_t distribution have been noticed in the South Equatorial Current and Somali regions when compared with the distribution of σ_t at 20 and 50 m. The σ_t surface slopes downward from approximately 5°S to 20°S; the σ_t values range from approximately 26.3 at 5°S to 24.8 at 20°S. Closed isolines of σ_t, indicating the presence of a clockwise gyre, are noticed off the African coast at 150 m. At 300, 500 and 1000 m (Figure 14(d)–(f)), the σ_t values are more smoothed with negligible gradient observed in the entire model domain.

4.3.2. Computed sea surface topography and circulation. The computed mean sea surface topography during Spring is presented in Figure 15. Sea surface topography pattern shows the presence of a zonally oriented ridge between 5°S and 20°S. The heavy packing of sea surface topography contours along the East African and Somali coasts shows the presence of strong currents along these regions. The sea surface topography contours also show the presence of four permanent surface currents, such as the westward-flowing SEC between 5°S and 20°S, the northward-flowing EACC, the northeastward-flowing SC and the Southwest Monsoon Drift Current that encompasses the Arabian Sea.

The computed currents at 20, 50, 150, 300, 500 and 1000 m are depicted in Figure 16(a)–(f). The Spring mean current pattern at 20 m (Figure 16(a)) shows the presence of westward and southwestward-flowing SEC in the southern tropical Indian Ocean between 5°S and 20°S. This current (SEC) is mainly driven by the prevailing Southwest trades in this region. The SEC attains velocities of about 75 cm s^{-1} at the southern part. The SEC, on reaching the East African coast, feeds initially the EACC and subsequently the northeastward-flowing SC. The magnitude of the SC reaches about 1 m s^{-1}. An eastward-flowing equatorial current known as the Equatorial Jet (EJ) is seen between the equator and 5°S, east of 50°E. Occurrence of the EJ in the tropical Indian Ocean during the transition period has been reported first by Wyrtki [18], and Molinari *et al.* [19] also observed the same in the monthly climatology of surface currents using surface drifting buoy data. The Arabian Sea north of the equator is mainly covered by southeastward and southward-flowing monsoon current. The computed currents at 20 m are consistent with the ship drift currents compiled by Cutler and Swallow [15] (Figure 17).

The circulation features at 50 m are shown in Figure 16(b). The SEC, which has become more zonal compared with its pattern at the surface, flows westward between 8°S and 20°S and turns northwards at the east coast of Madagascar. The northward-flowing coastal current along the east coast of Madagascar feeds into the northward-flowing SC via the EACC, after travelling westward at the northern tip of Madagascar. Another important feature of circulation at 50 m is the presence of a clockwise eddy between 5°S and 5°N off the Somali coast. Figure 16(b) also shows an eastward flowing equatorial undercurrent between 3°N and 5°S east of 50°E. A northward-flowing coastal undercurrent can be seen all along the west coast of India. This flow is primarily a geostrophic current caused by the upward slope of the sea level towards the west coast of India.

The computed currents at 150 and 300 m are presented in Figure 16(c) and (d) respectively. The circulation pattern at these two depths is not significantly different from what was

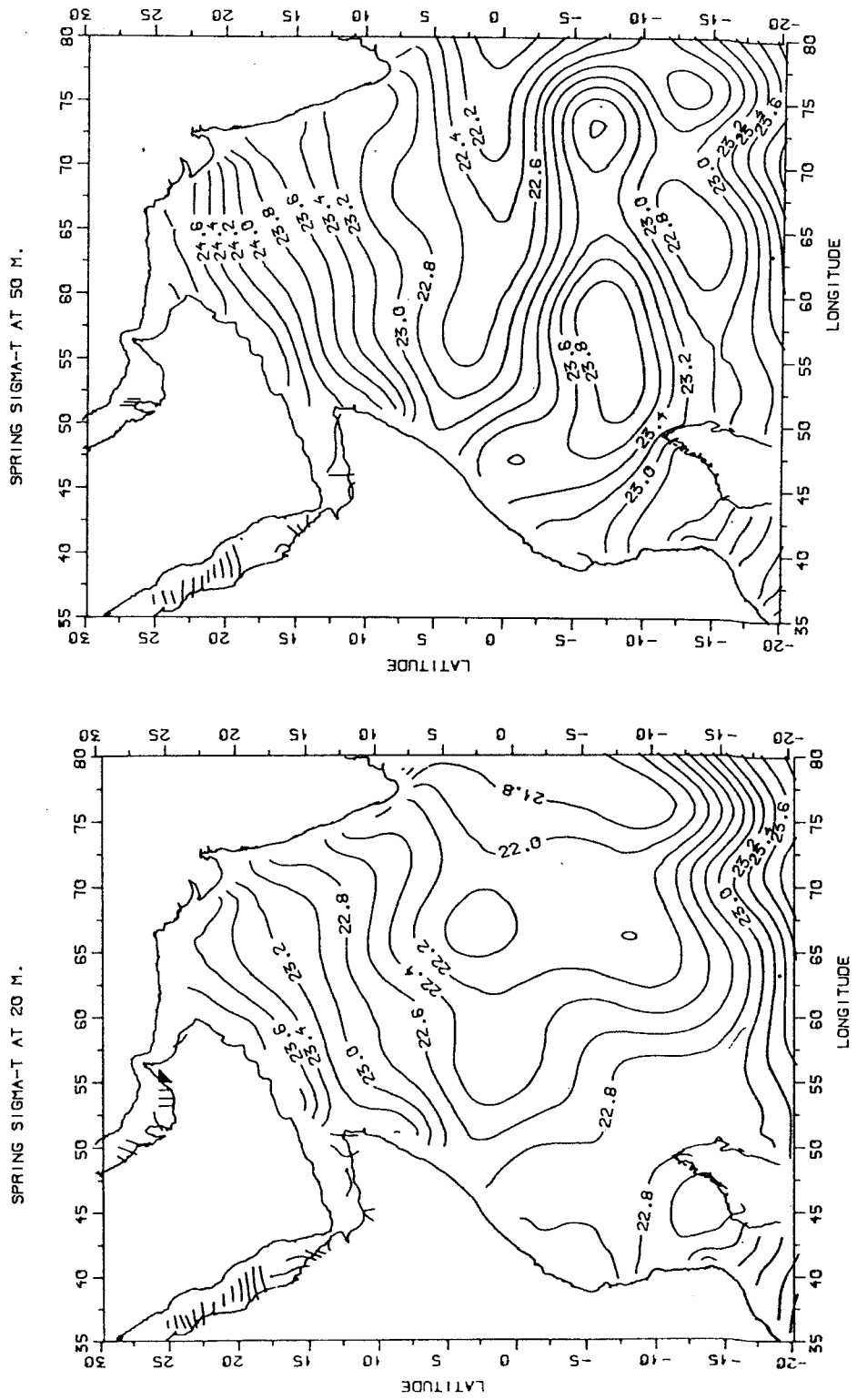

Figure 14. Spatial distribution of σ_t during Spring at (a) 20 m, (b) 50 m, (c) 150 m, (d) 300 m, (e) 500 m and (f) 1000 m.

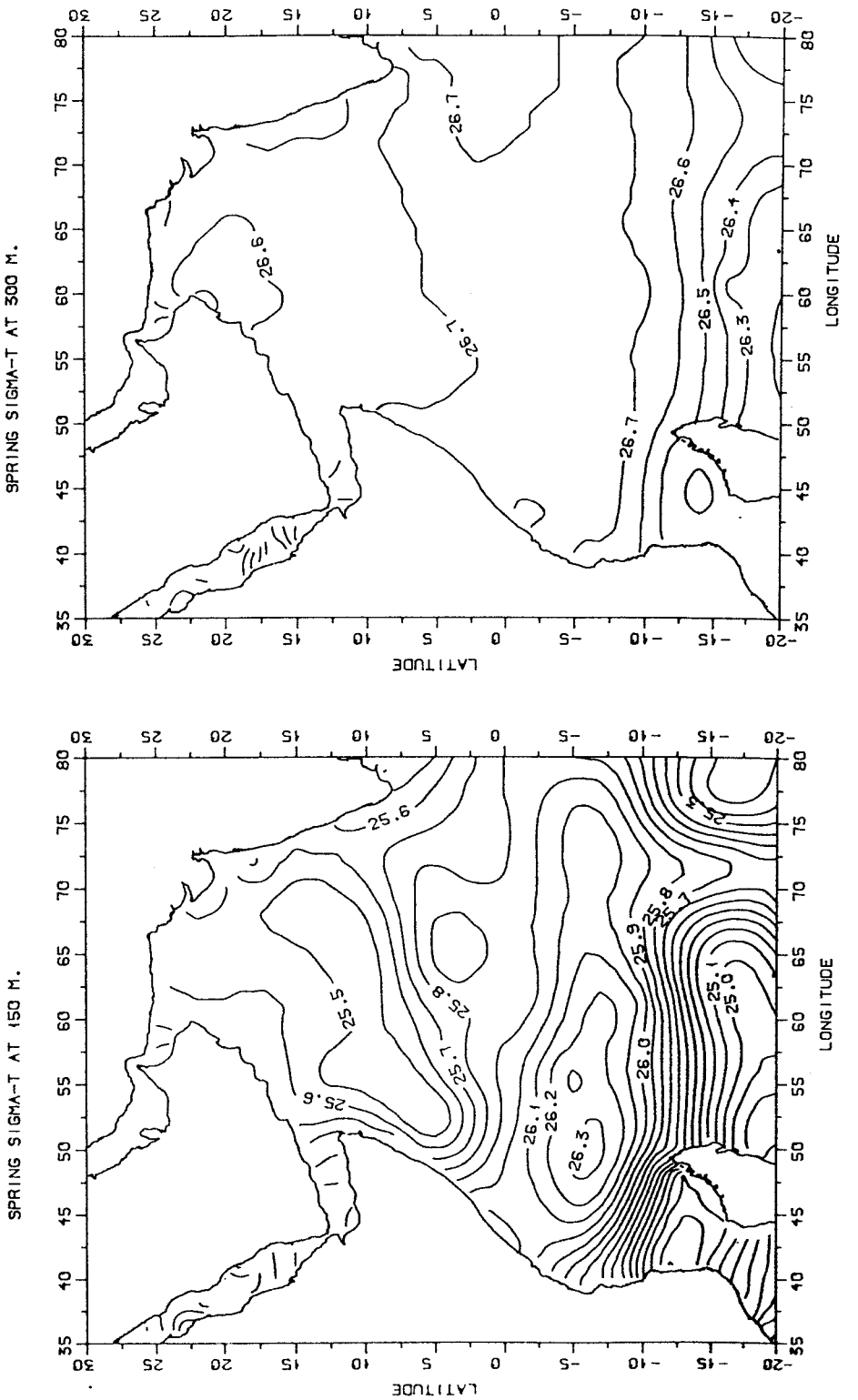

Figure 14 (*Continued*)

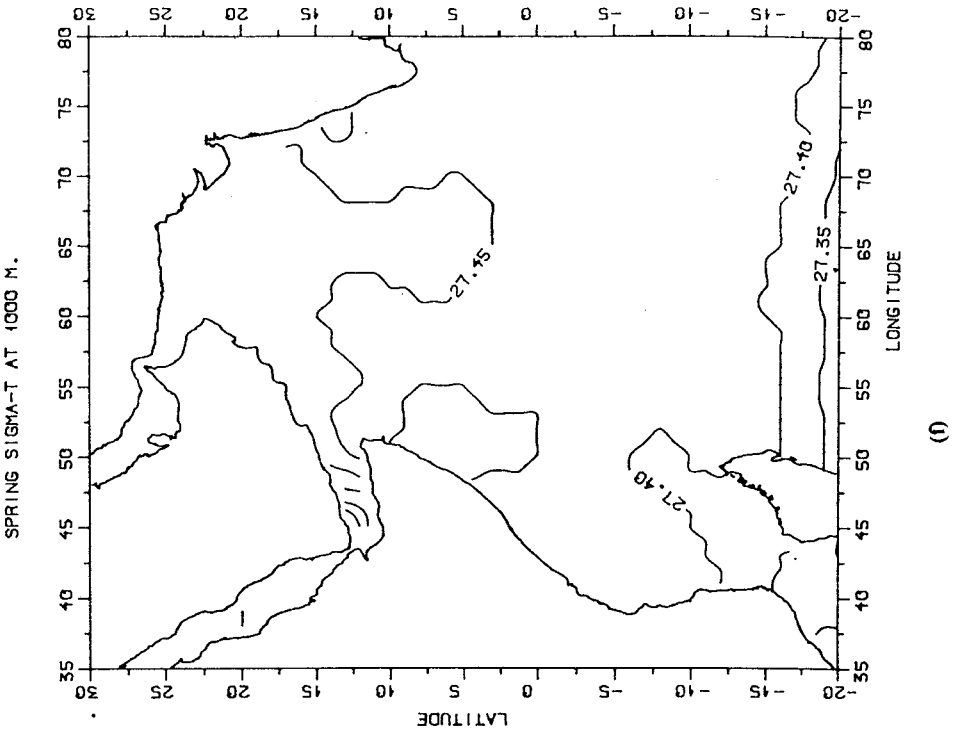

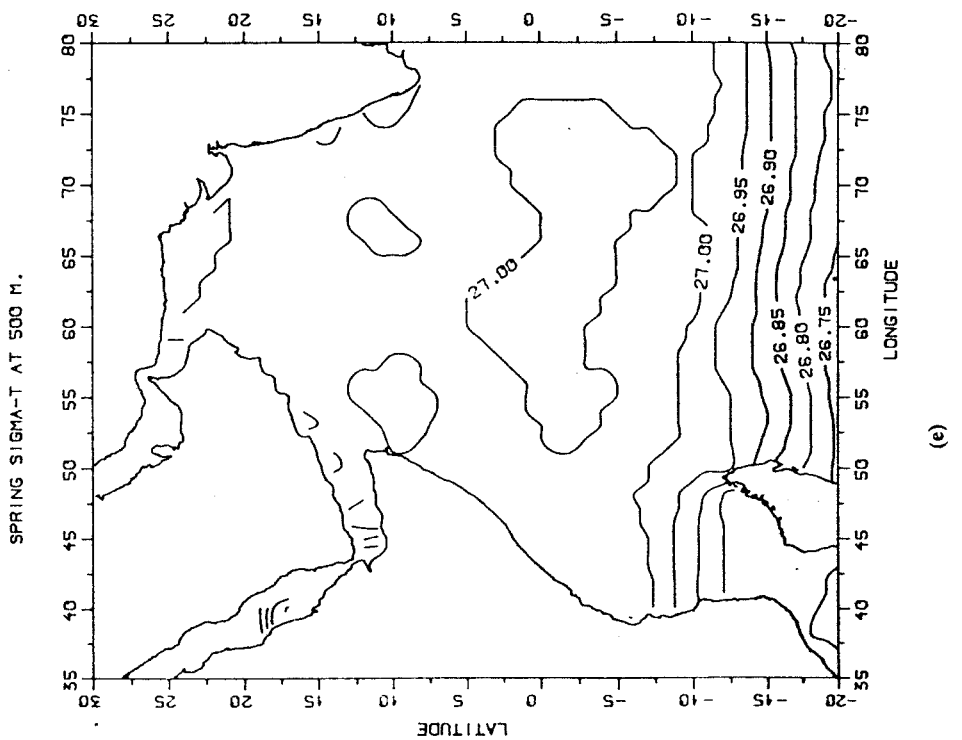

Figure 14 (*Continued*)

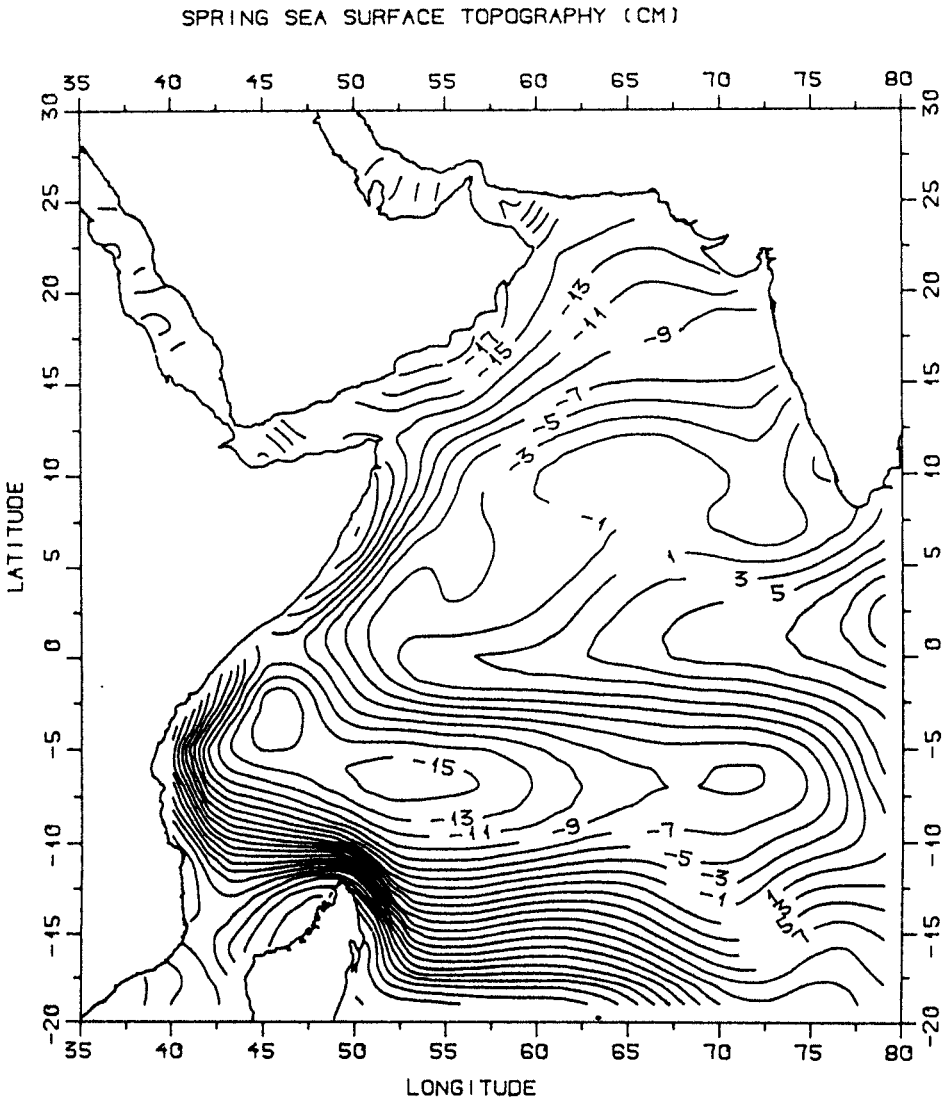

Figure 15. Computed sea surface topography (cm) during Spring.

observed at 50 m except that the magnitude of current is reduced and that the position of the eddy located off the Somali coast is shifted slightly southwards. The westward-flowing subsurface SEC could be seen 8°S and 20°S. The clockwise eddy found off the Somali coast is now located between the equator and 5°S. The strength of the westward-flowing SEC is approximately 10 cm s^{-1}. The eastward-flowing undercurrent that originates from approximately 50°E could be seen between 5°S and 2°N, and it continues up to the eastern part of the model area at 80°E. The magnitude of the narrow northward-flowing coastal undercurrent is slightly reduced, which is of the order of 5–10 cm s^{-1}. The current pattern at 300 m (Figure 16(d)) is almost analogous to what is observed at 150 m, the only difference being that the overall magnitude of the current is further reduced. The magnitude of the current in the northern Arabian Sea is of the order of 5 cm s^{-1}. The circulation patterns at 150 and 300 m are fully consistent with the sea surface topography pattern.

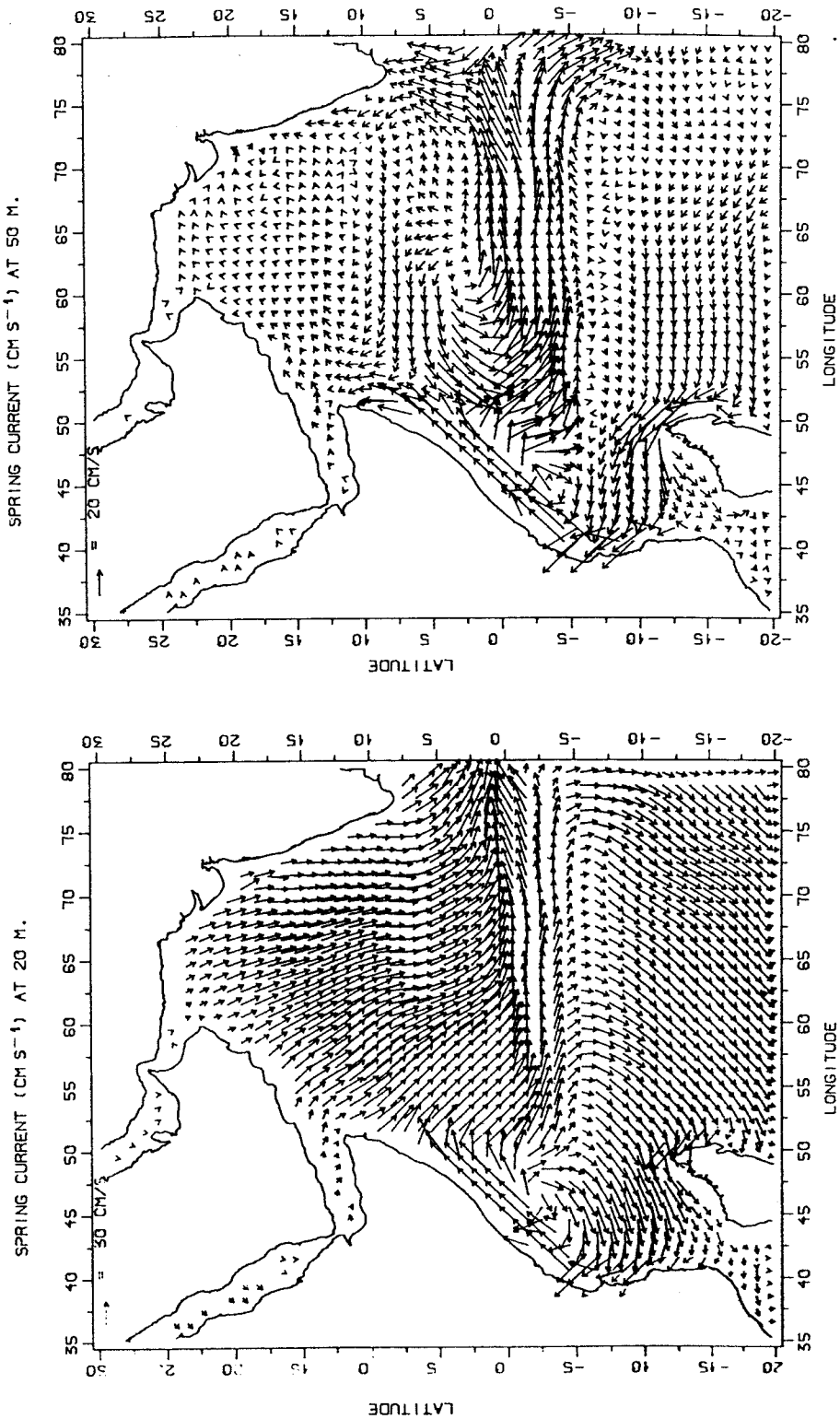

Figure 16. Computed current during Spring at (a) 20 m, (b) 50 m, (c) 150 m, (d) 300 m, (e) 500 m and (f) 1000 m.

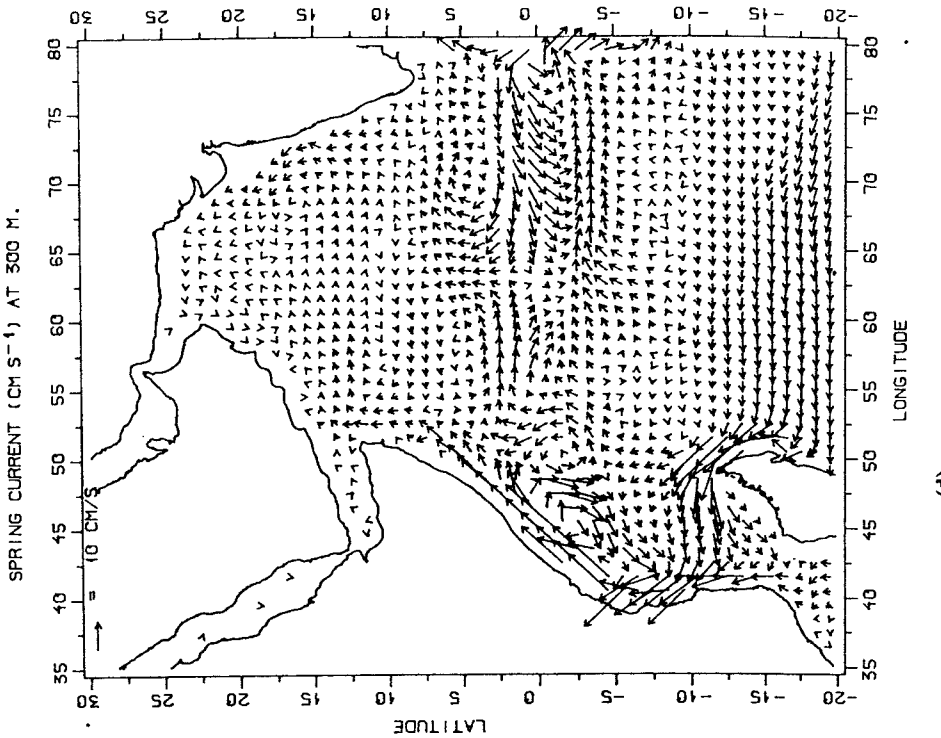

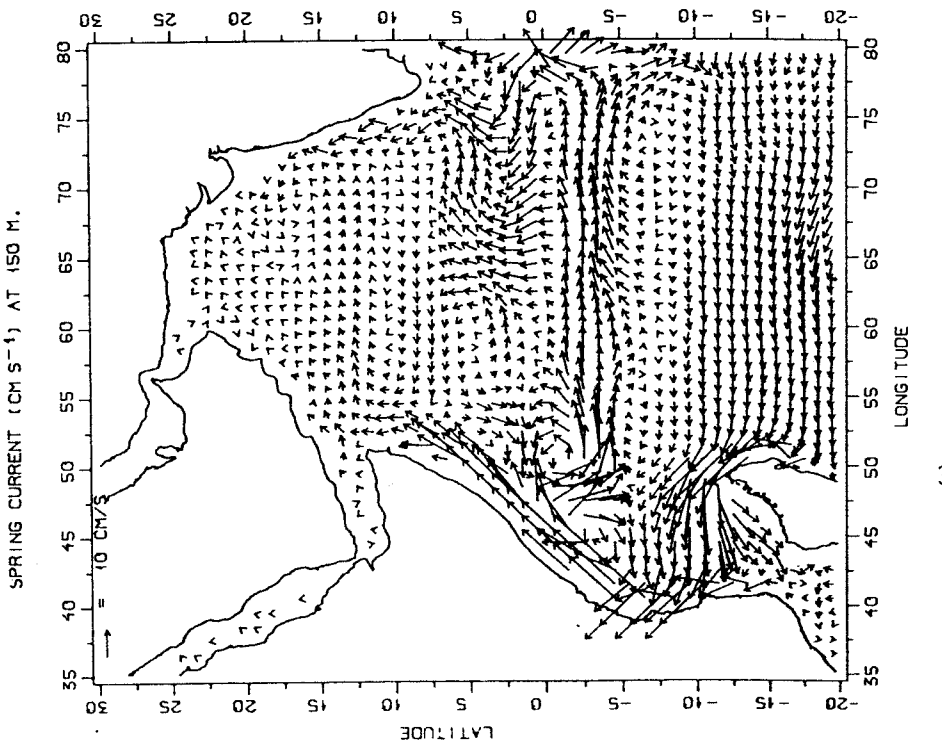

Figure 16 (*Continued*)

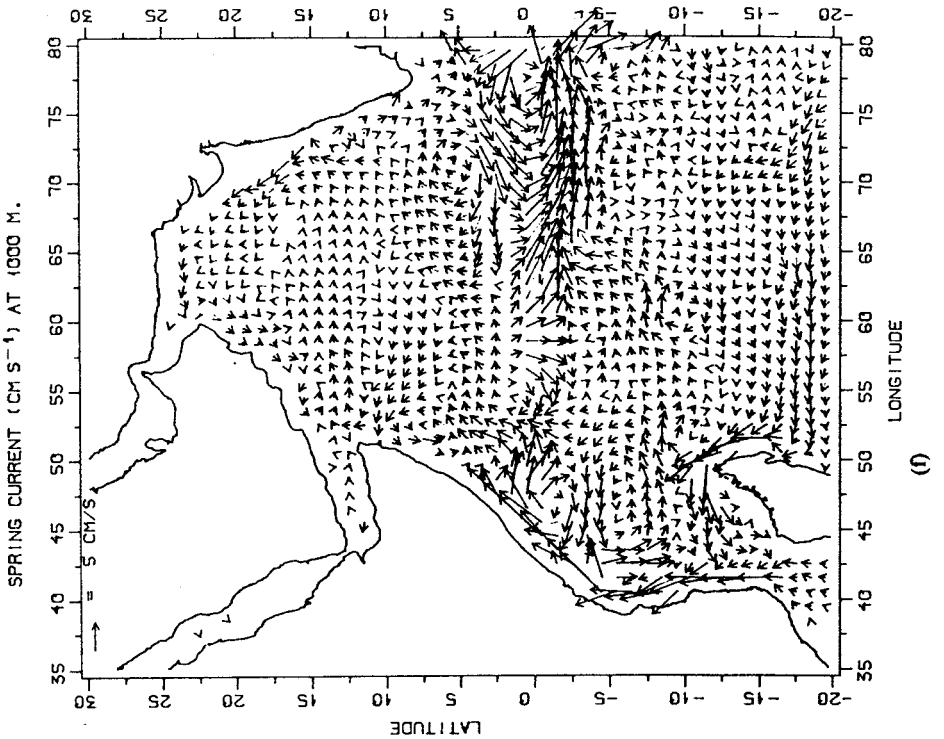

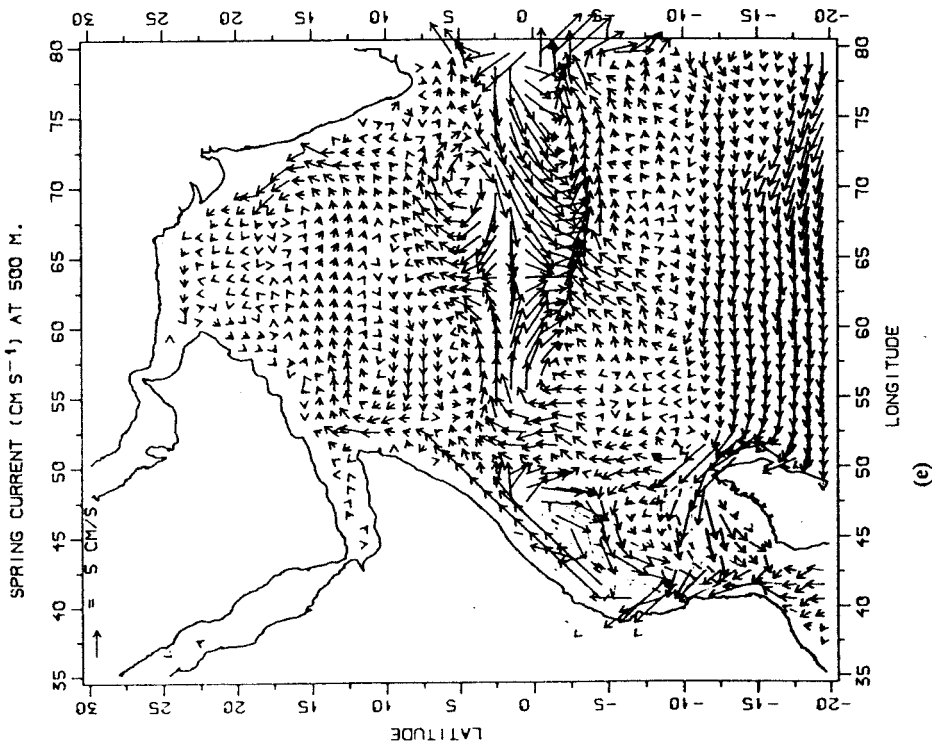

Figure 16 (*Continued*)

The mean currents at 500 and 1000 m are presented in Figure 16(e) and (f) respectively. A broad cyclonic gyre-type of circulation is found in the northern Arabian Sea at both these depths. At 500 m, the SEC has shifted more to the south (Figure 16(e)). The SEC now extends between 12°S and 20°S. At 1000 m, the intensity of current is further reduced compared with that at 500 m.

4.3.3. Adjustment of temperature and salinity fields. The diagnostic calculation of currents suffers from two main disadvantages: (1) the available climatic temperature and salinity fields contain noise effects of stationary processes; (2) the density field is not in adjustment with wind and bottom relief of the ocean. To overcome this difficulty, in our semi-diagnostic model, we imposed the specified temperature and salinity field and flow field calculated by the diagnostic

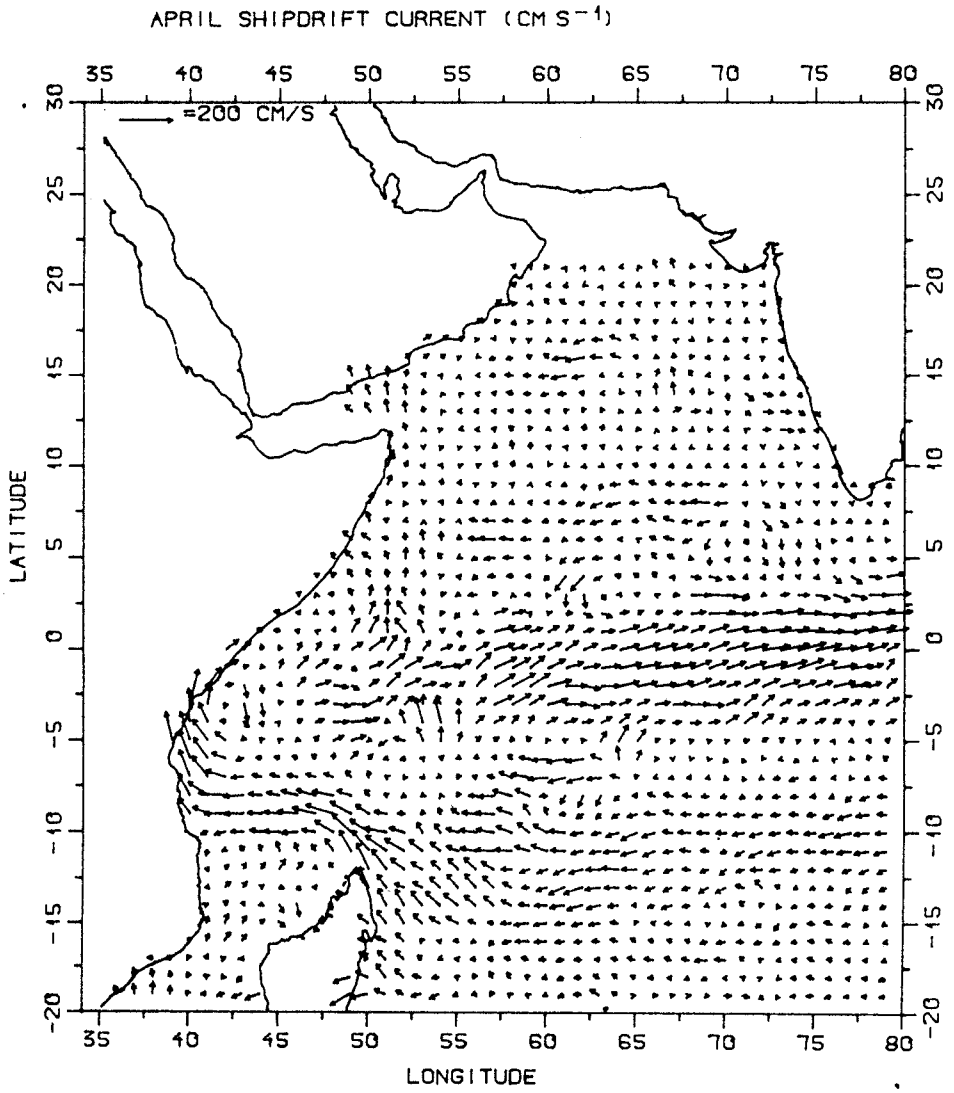

Figure 17. The ship drift surface current of Cutler and Swallow [15] during April.

method as initial approximations for the adjustment process. The climatic temperature and salinity fields were found to be hydrodynamically adjusted after 30 days of model integration from the diagnostic stage. The hydrodynamic adjustment of temperature and salinity fields at selected depths of 20, 50, 150 and 300 m are presented in the form of anomaly diagrams. The anomaly of a particular variable (temperature/salinity) is equal to the difference between the observed variable and adjusted variable.

The temperature and salinity anomaly fields at 20, 50, 150 and 300 m are presented in Figures 18(a)–(d) and 19(a)–(d) respectively. Analysis of temperature anomaly fields at all depths shows that the climatic temperature, which was used as initial conditions in the semi-diagnostic model, was hydrodynamically smoothed during the adjustment process. At 20 m, the temperature anomaly field increases from 0.2°C at 17°S to approximately 1°C at the equatorial regions; the maximum anomaly of about 2°C is noticed off the Somali coast, which is the region of upwelling during the pre-monsoon season. There is also a gradual increase in the temperature anomaly field from the west coast of India to the central part of the Arabian Sea. At 50 m, north of 22°N, the anomaly field is zero, indicating that there is no deviation between climatic temperature and adapted temperature. Off the Somali region, the temperature anomaly reaches a high value of 2°C. In the northern hemisphere, the temperature anomaly is found to be decreasing northwards from the equatorial regions.

At 150 m depth, the maximum positive temperature anomaly is observed off the Somali coast, where its value reaches about 1.5°C. The temperature anomaly is negative off the central and eastern Arabian Sea. At 300 m, a negative temperature anomaly is found in the southern tropical Indian Ocean. A positive temperature anomaly of 0.2–0.4°C is noticed in the northern Arabian Sea.

The adapted salinity at 20 m shows that significant changes in the salinity values in the central Arabian Sea take place (Figure 19(a)). South of 15°S, the salinity anomaly is zero, indicating that there is no deviation between the observed and adapted salinity values. The maximum positive salinity anomaly of 0.10 is seen in the Somali region. At 50 m (Figure 19(b)), a positive salinity anomaly ranging from 0.05 to 0.10 is observed in the Arabian Sea north of the equator. Along the coastal regions of Africa and Somalia, salinity anomaly reaches a value of 1.0. A maximum negative salinity anomaly of 1.0 is observed in the southern tropical and equatorial Indian Ocean. The Spring salinity anomaly at 150 and 300 m are presented in Figure 19(c) and (d) respectively. These two figures show that there is no significant change in the salinity anomaly at greater depths. The salinity anomaly decreases with depth, indicating that the deviation from the observed and adapted values are negligible at greater depths. At 300 m, the salinity anomaly is practically zero in the equatorial belt between 10°N and 10°S.

5. CONCLUSIONS

Numerical experiments have been performed using an adaptation model to compute the climatic mean circulation in the western part of tropical Indian Ocean. The most appropriate parameter values obtained from the sensitivity experiments, with an 18-level adaptation model, for the realistic calculation of climatic mean currents in the model area are: 5×10^8 cm^2 s^{-1} for the horizontal friction and diffusivity coefficients, 10 cm^2 s^{-1} for the vertical friction and diffusivity coefficients. These experiments also show that the surface circulation is mainly controlled by the wind stress forcing, and thermohaline forcing (density) plays a minor role. At the subsurface and deeper levels, in addition to the thermohaline forcing, the circulation is

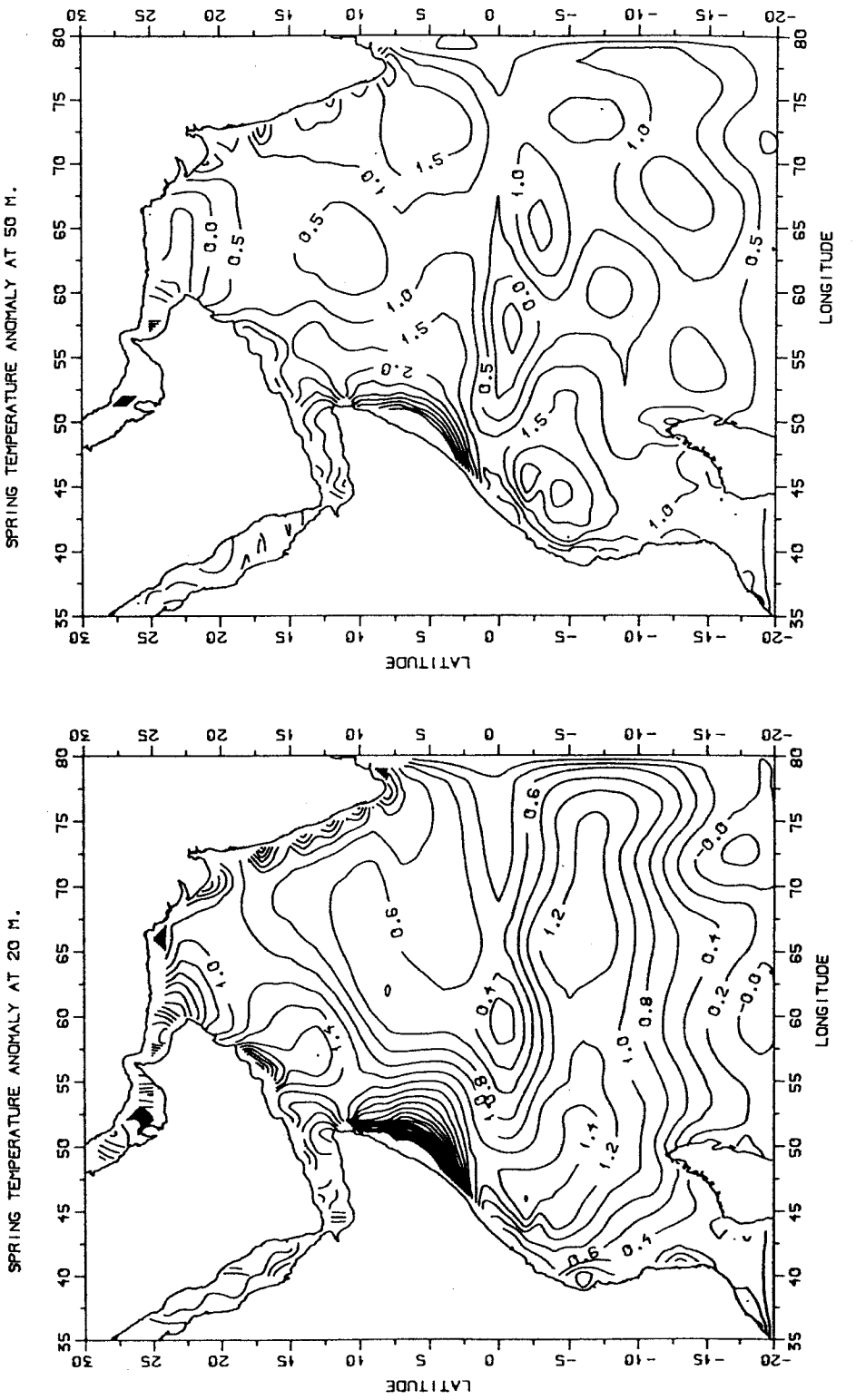

Figure 18. Temperature anomaly fields during Spring at (a) 20 m, (b) 50 m, (c) 150 m and (d) 300 m.

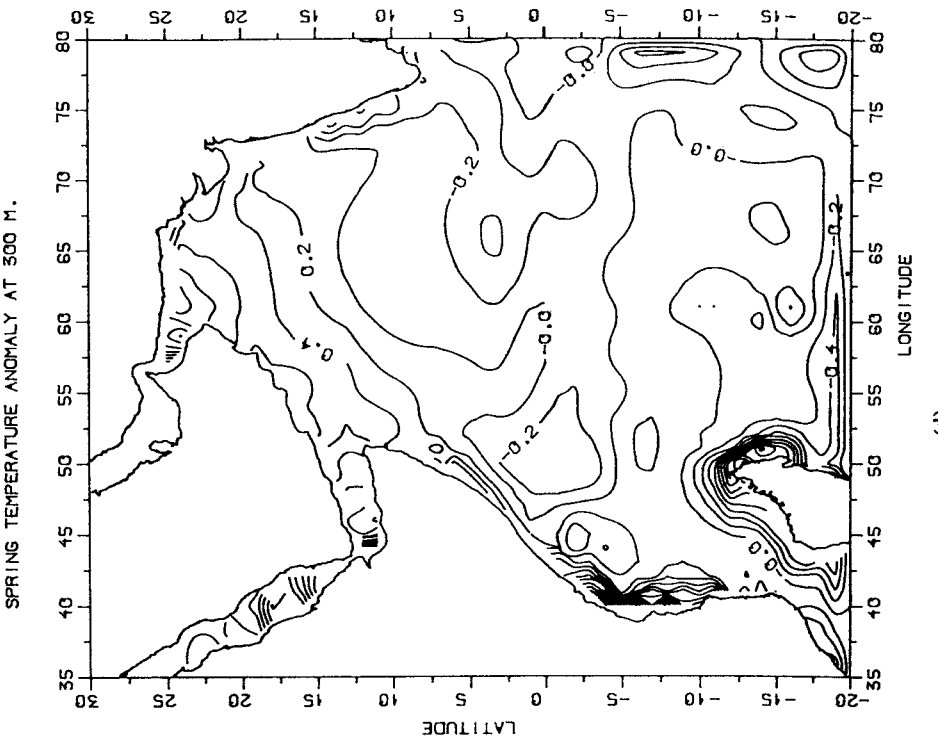

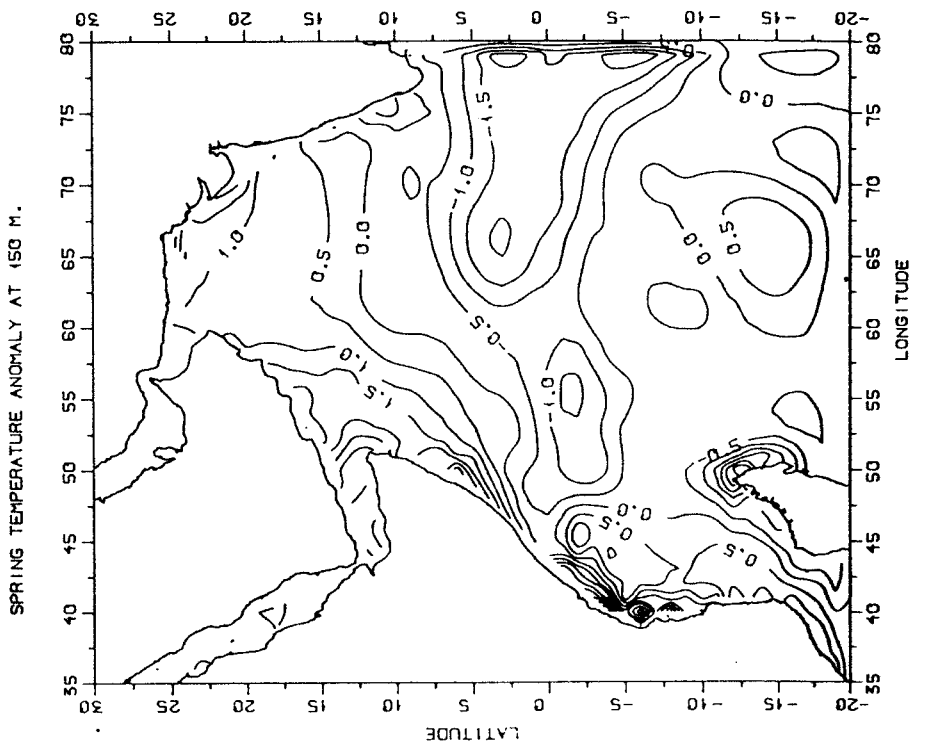

Figure 18 (*Continued*)

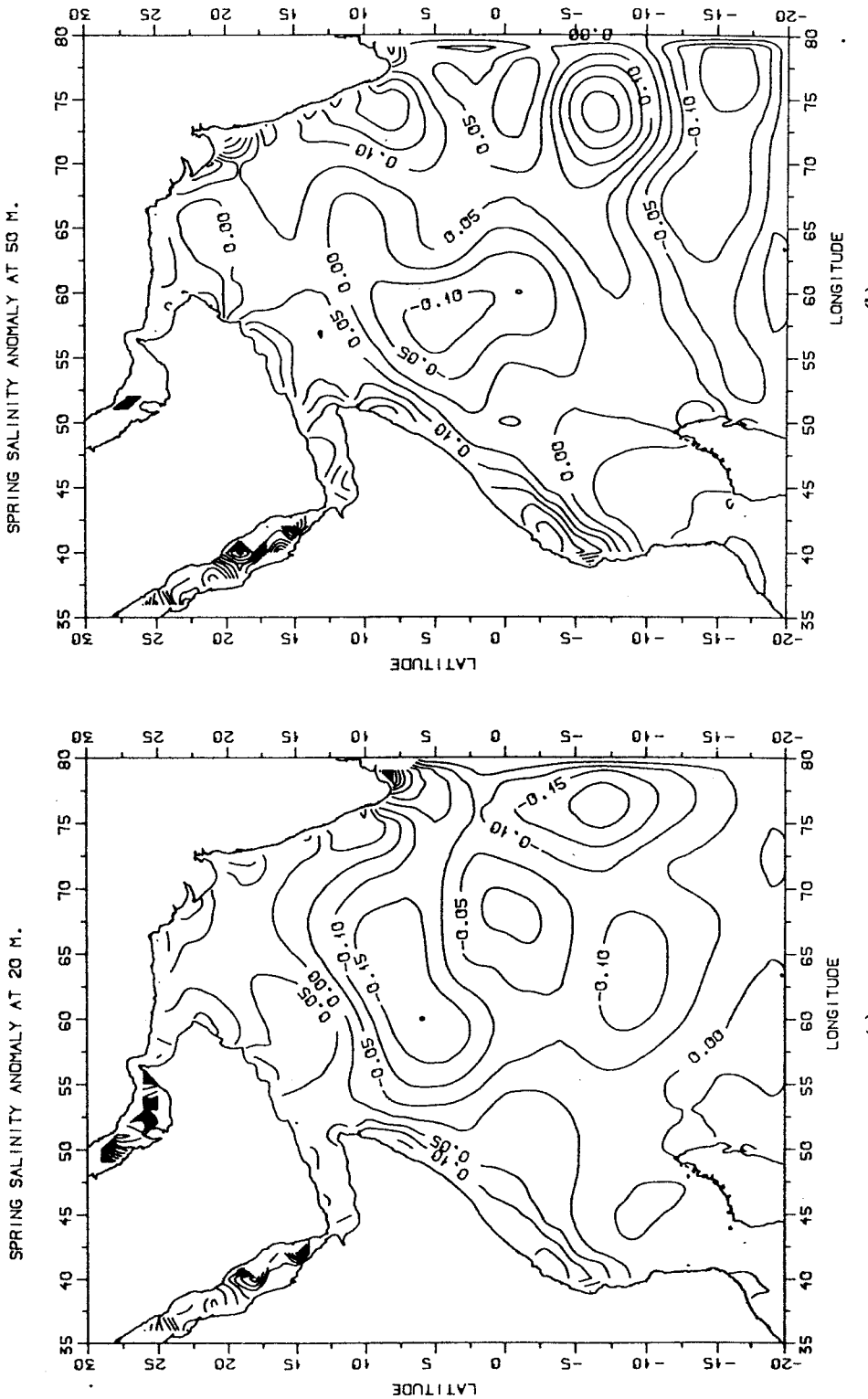

Figure 19. Salinity anomaly fields during Spring at (a) 20 m, (b) 50 m, (c) 150 m and (d) 300 m.

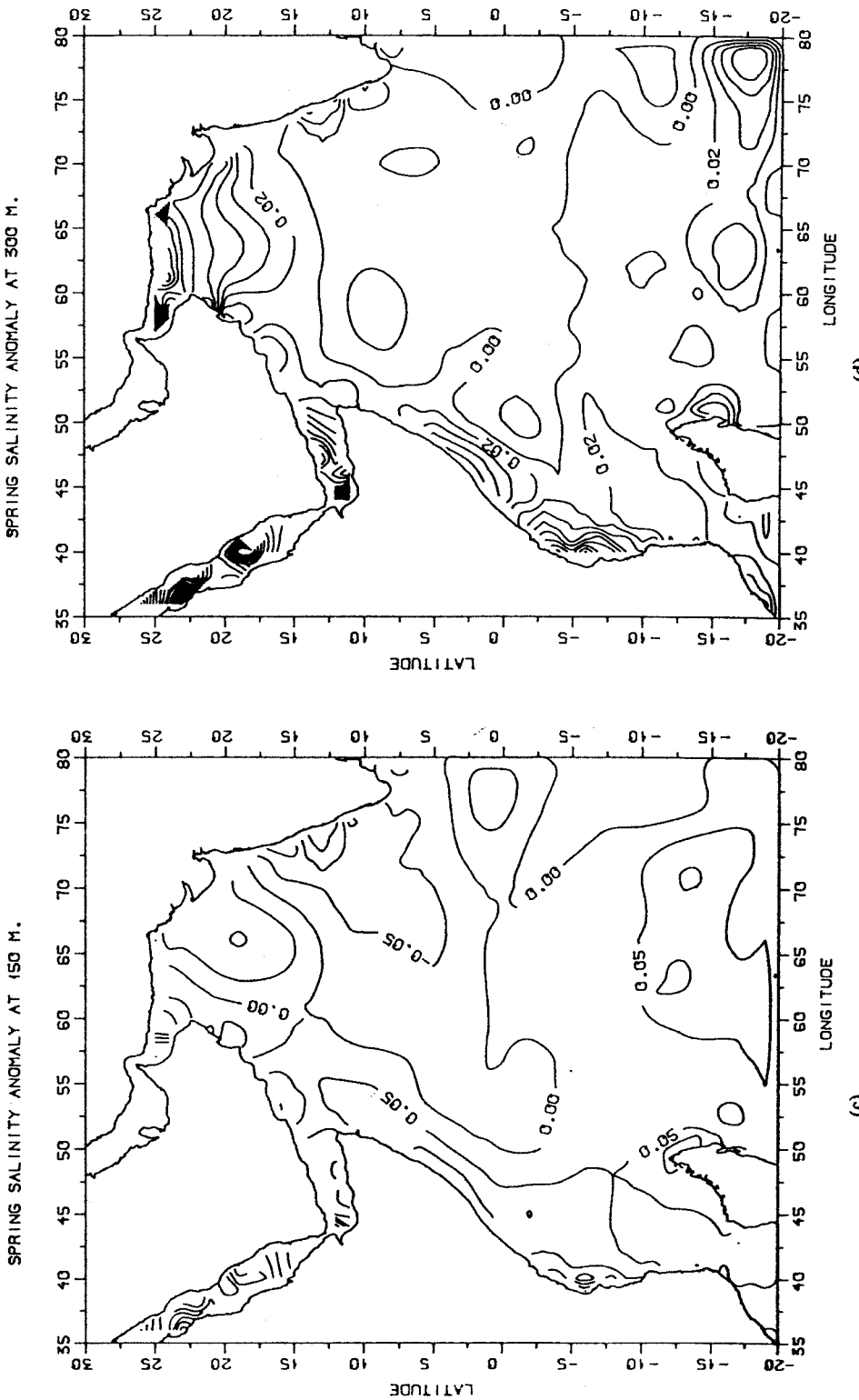

Figure 19 (*Continued*)

mainly controlled by the sea surface topography. The circulation features computed by the 33-level adaptation model were explained in terms of the forcing considered in the model and were compared with available observations on currents in the model area. The model has been successful in reproducing all the permanent current systems in the tropical Indian Ocean, which are mainly controlled by the local forcing of surface wind, density and sea surface topography.

APPENDIX A

A.1. Finite difference formulation

The model equations (1)–(7) are solved subject to the boundary and initial conditions mentioned in Section 2.2 using a leap-frog numerical scheme. While approximating the system (1)–(7) by a finite difference technique, second-order accuracy in spatial variables was achieved; the finite difference scheme also satisfies the main conservation laws used in the original system of equations. The model area was approximated by a set of boxes with equal horizontal axis, with the velocity vector computed at its centre and the temperature and salinity computed at the lateral boundaries of the box as shown in Figure 2. The vertical velocity is determined at equal distances between the nodal values T_k and T_{k+1}, and the sea level is obtained at the sea surface $z = 0$. While the Coriolis term is treated in a semi-implicit fashion, the friction terms are calculated at the backward time level. All other terms in the equations are calculated at the central time level. To inhibit the time splitting instability normally encountered in the leap-frog scheme, a Matsuno scheme, which averages solution at two consecutive time steps, was employed at every 24 time steps.

Let us denote the number of boxes as $K_{i,j}$. Then, the depth at the node (i, j) is equal to: $H_{i,j} = \Sigma_{k=1}^{K_{i,j}} \Delta Z_{k+1/2}$ and the number of levels at any grid point can be found from:

$$H_{i,j} = \max(K_{i,j}, K_{i+1}, K_{i,j+1}, K_{i+1,j+1}).$$

Before describing the finite difference scheme, we first define the operators of finite difference differentiation and averaging as follows:

$$\delta_\lambda f = \frac{\left[f\left(\lambda + \frac{\Delta\lambda}{2}\right) - f\left(\lambda - \frac{\Delta\lambda}{2}\right)\right]}{\Delta x}, \tag{A1a}$$

$$\bar{f}^\lambda = \frac{\left[f\left(\lambda + \frac{\Delta\lambda}{2}\right) + f\left(\lambda - \frac{\Delta\lambda}{2}\right)\right]}{2}. \tag{A1b}$$

Considering Equation (A1), the advection operators in the momentum, heat and salt transport equations are approximated as follows:

$$A^{\mathrm{V}} f = \frac{1}{R \sin\theta}\left[\delta_\lambda(\bar{u}^\lambda \bar{f}^\lambda) + \delta_\theta(\overline{v \sin\theta}^\theta \bar{f}^\theta)\right] + \delta_z(w^{\mathrm{V}} \bar{f}^z), \tag{A2a}$$

$$A^{\mathrm{T}} f = \frac{1}{R \sin\theta}\left[\delta_\lambda(\bar{u}^\theta \bar{f}^\lambda) + \delta_\theta(\overline{v \sin\theta}^\lambda \bar{f}^\theta)\right] + \delta_z(w^{\mathrm{T}} \bar{f}^z), \tag{A2b}$$

$$A^{\mathrm{S}} f = \frac{1}{R \sin\theta}\left[\delta_\lambda(\bar{u}^\theta \bar{f}^\lambda) + \delta_\theta(\overline{v \sin\theta}^\lambda \bar{f}^\theta)\right] + \delta_z(w^{\mathrm{S}} \bar{f}^z). \tag{A2c}$$

The Laplacian operator, Δ, is approximated as

$$\Delta f = \frac{1}{R^2 \sin^2\theta}\,[\delta_\lambda(\delta_\lambda f)] + \frac{1}{(R^2 \sin\theta)}\,\delta_\theta(\delta_\theta f \sin\theta). \tag{A3}$$

The friction terms F^λ and F^θ in the momentum equations are defined as follows:

$$D^{\mathrm{u}}u = \delta_z(v\delta_z u) + \mu\left[\frac{1}{R^2 \sin^2\theta}\,\delta_\lambda(\delta_\lambda u) + \frac{1}{R^2 \sin\theta}\,\delta_\theta(\sin\theta\delta_\theta u)\right] - \mu\left[\frac{u}{R^2 \sin^2\theta} - \frac{2\cos\theta}{R^2 \sin^2\theta}\,\delta_\lambda v\right], \tag{A4a}$$

$$D^{\mathrm{v}}v = \delta_z(v\delta_z v) + \mu\left[\frac{1}{R^2 \sin^2\theta}\,\delta_\lambda(\delta_\lambda v) + \frac{1}{R^2 \sin\theta}\,\delta_\theta(\sin\theta\delta_\theta v)\right] - \mu\left[\frac{v}{R^2 \sin^2\theta} - \frac{2\cos\theta}{R^2 \sin^2\theta}\,\delta_\lambda u\right]. \tag{A4b}$$

The turbulent diffusion terms in the heat and salt transport equations are defined as follows:

$$D^{\mathrm{T}}T = \delta_z(v_T\delta_z T) + \mu_T\left[\frac{1}{R^2 \sin^2\theta}\,\delta_\lambda(\delta_\lambda T) + \frac{1}{R^2 \sin\theta}\,\delta_\theta(\sin\theta\delta_\theta T)\right], \tag{A5a}$$

$$D^{\mathrm{S}}S = \delta_z(v_T\delta_z S) + \mu_T\left[\frac{1}{R^2 \sin^2\theta}\,\delta_\lambda(\delta_\lambda S) + \frac{1}{R^2 \sin^2\theta}\,\delta_\theta(\sin\theta\delta_\theta S)\right]. \tag{A5b}$$

The hydrostatic equation is represented by:

$$P_{i+1/2,\,j+1/2,k} = \rho_0 g \zeta_{i+1/2,\,j+1/2} + g\sum_{k=1}^{k} \bar{\rho}'^{z}\Delta z_k. \tag{A6}$$

Considering Equations (A1)–(A6), the finite difference approximation of the original system of equations (1)–(7) is written as follows:

$$\delta_t u_{i,j,k} + A^{\mathrm{v}}u^n + l\frac{(v^{n+1} + v^{n-1})}{2} + \frac{\cot\theta}{R}\,(uv)^n = -\frac{g}{R\sin\theta}\,[\delta_\lambda\zeta^\theta]^n - \frac{g}{\rho_0 R\sin\theta}\left[\delta_\lambda\left(\sum_{k=1}^{k}\bar{\rho}'^{\theta z}\Delta z_k\right)\right]^n + D^{\mathrm{u}}u^{n-1}, \tag{A7}$$

$$\delta_t v_{i,j,k} + A^{\mathrm{v}}v^n - l\frac{(u^{n+1} + u^{n-1})}{2} - \frac{\cot\theta}{R}\,(u^2)^n = -\frac{g}{R}\,[\delta_\theta\zeta^\theta]^n - \frac{g}{\rho_0 R}\left[\delta_\theta\left(\sum_{k=1}^{k}\bar{\rho}'^{\lambda z}\Delta z_k\right)\right]^n + D^{\mathrm{v}}v^{n-1}, \tag{A8}$$

$$\frac{1}{R\sin\theta}\,[\delta_\lambda\bar{u}^\theta + \delta_\theta(\overline{v\sin\theta}^\lambda)] + \delta_z w = 0, \tag{A9}$$

$$\delta_t T_{i+1/2,\,j+1/2,k} + A^{\mathrm{T}}T^n = D^{\mathrm{T}}T^{n-1}, \tag{A10}$$

$$\delta_t S_{i+1/2,\,j+1/2,k} + A^{\mathrm{S}}S^n = D^{\mathrm{S}}S^{n-1}. \tag{A11}$$

In Equations (A7)–(A11), n is the time step number. The semi-implicit representation of the Coriolis force would enable us to integrate the model equations with larger time steps.

A.2. Sea surface topography (sea level) equation

In order to have a closed system of equations in seven unknowns, it is necessary to derive an expression for sea surface topography. Sea surface topography is a dynamical variable intimately linked to the flow fields in the upper mixed and thermocline layers. While the upper mixed layer circulation is essentially controlled by the resultant of wind stress and sea surface slope, the circulation in the thermocline is mainly controlled by the sea surface topography. The slope of the sea surface affects the slope of the thermocline, which in turn affects the thermocline circulation.

A detailed discussion on the various methods of derivation of sea surface topography is given in the works of Demin and Ibraev [11]. In this paper, the sea surface topography equation is derived based on the solutions of the finite difference equations of momentum, hydrostatics and continuity. The finite difference equations (Equations (A7)–(A9)) are solved by a leap-frog numerical scheme. The two-dimensional integral continuity equation, which is the equation for sea surface topography at the internal grid points, is obtained by summing up the equation of continuity along all the levels, taking into consideration the boundary condition for vertical velocity ($w = 0$) at the surface and bottom. By applying the lateral boundary conditions for velocity fields, the equation for sea surface topography at the solid boundary points are also obtained.

To obtain the solution of the finite difference equations (A7) and (A8), we first make the following substitutions:

$$R_\lambda = -\frac{g}{\rho_0 R \sin\theta}\left(\sum_{k=1}^{K} \delta_\lambda \bar{\rho}'^{\theta z} \Delta z_k\right)^n - \frac{\cot\theta}{R}(uv)^n - A^{\mathrm{v}} u^n + D^{\mathrm{u}} u^{n-1},$$

$$R_\theta = -\frac{g}{\rho_0 R}\left(\sum_{k=1}^{K} \delta_\theta \bar{\rho}'^{\lambda z} \Delta z_k\right)^n + \frac{\cot\theta}{R}(u^2)^n - A^{\mathrm{v}} v^n + D^{\mathrm{v}} v^{n-1}.$$

Considering the two substitutions, Equations (A7) and (A8) are transformed as follows:

$$\frac{u^{n+1} - u^{n-1}}{2T} + l\frac{(v^{n+1} + v^{n-1})}{2} = -\frac{g}{R\sin\theta}(\delta_\lambda \bar{\zeta}^\theta)^n + R_\lambda, \tag{A12}$$

$$\frac{v^{n+1} - v^{n-1}}{2T} - l\frac{(u^{n+1} + u^{n-1})}{2} = -\frac{g}{R}(\delta_\theta \bar{\zeta}^\lambda)^n + R_\theta. \tag{A13}$$

Equations (A12) and (A13) can further be simplified as follows:

$$\frac{u^{n+1}}{2T} + \frac{lv^{n+1}}{2} = -\frac{g}{R\sin\theta}(\delta_\lambda \bar{\zeta}^\theta)^n + R'_\lambda, \tag{A14}$$

$$\frac{v^{n+1}}{2T} - \frac{lu^{n+1}}{2} = -\frac{g}{R}(\delta_\theta \bar{\zeta}^\lambda)^n + R'_\theta, \tag{A15}$$

where

$$R'_\lambda = R_\lambda + \frac{u^{n-1}}{2T} - \frac{lv^{n-1}}{2} \quad \text{and} \quad R'_\theta = R_\theta + \frac{v^{n-1}}{2T} + \frac{lu^{n-1}}{2}.$$

System (A14) and (A15) is solved for u^{n+1} and v^{n+1} as follows:

$$u^{n+1} + Tlv^{n+1} = \frac{-2Tg}{R\sin\theta}(\delta_\lambda \bar{\zeta}^\theta)^n + 2TR'_\lambda, \tag{A16}$$

$$v^{n+1} - Tlu^{n+1} = \frac{-2Tg}{R}(\delta_\theta \bar{\zeta}^\lambda)^n + 2TR'_\theta. \tag{A17}$$

Equation (A16) can be written as

$$u^{n+1} = -Tlv^{n+1} - \frac{2Tg}{R\sin\theta}(\delta_\lambda \bar{\zeta}^\theta)^n + 2TR'_\lambda.$$

Substituting the value of v^{n+1} from Equation (A17) into the above equation, we get

$$u^{n+1} = -Tl\left[Tlu^{n+1} - \frac{2Tg}{R}(\delta_\theta \bar{\zeta}^\lambda)^n + 2TR'_\theta\right] - \frac{2Tg}{R\sin\theta}(\delta_\lambda \bar{\zeta}^\theta)^n + 2TR'_\lambda$$

or

$$u^{n+1} + T^2l^2u^{n+1} = \frac{2T^2lg}{R}(\delta_\theta \bar{\zeta}^\lambda)^n - 2T^2lR'_\theta - \frac{2Tg}{R\sin\theta}(\delta_\lambda \bar{\zeta}^\theta)^n + 2TR'_\lambda.$$

Simplifying the above equation, we get the final equation for u^{n+1} as follows:

$$u^{n+1} = \frac{1}{(1+T^2l^2)}\left[\frac{-2Tg}{R\sin\theta}(\delta_\lambda \bar{\zeta}^\theta)^n + 2TR'_\lambda - Tl\left(\frac{-2Tg}{R}(\delta_\theta \bar{\zeta}^\lambda) + 2TR'_\theta\right)\right]. \tag{A18}$$

From Equation (A17), we have

$$v^{n+1} = Tlu^{n+1} - \frac{2Tg}{R}(\delta_\theta \bar{\zeta}^\lambda)^n + 2TR'_\theta.$$

Substituting the value of u^{n+1} from Equation (A16) into the above equation, we get

$$v^{n+1} = Tl\left[-Tlv^{n+1} - \frac{2Tg}{R\sin\theta}(\delta_\lambda \bar{\zeta}^\theta)^n + 2TR'_\lambda\right] - \frac{2Tg}{R}(\delta_\theta \bar{\zeta}^\lambda)^n + 2TR'_\theta,$$

$$v^{n+1} = -T^2l^2v^{n+1} - \frac{2T^2lg}{R\sin\theta}(\delta_\lambda \bar{\zeta}^\theta)^n + 2T^2lR'_\lambda - \frac{2Tg}{R}(\delta_\theta \bar{\zeta}^\lambda)^n + 2TR'_\theta.$$

Simplifying the above equation, we get the final solution for v^{n+1} as follows:

$$v^{n+1} = \frac{1}{(1+T^2l^2)}\left[\frac{-2Tg}{R}(\delta_\theta \bar{\zeta}^\lambda)^n + 2TR'_\theta + Tl\left(\frac{-2Tg}{R\sin\theta}(\delta_\lambda \bar{\zeta}^\theta) + 2TR'_\lambda\right)\right]. \tag{A19}$$

The solution for u^{n+1} and v^{n+1} should be summed up over the vertical level k ($k = 1, \ldots, K_{i,j}$) to obtain the solution for the vertically integrated velocity components $\tilde{u}^{n+1}$ and $\tilde{v}^{n+1}$. The vertically integrated velocity components are defined as follows:

$$\tilde{u}_{i,j} = \sum_{k=1}^{K} u_{i,j}\Delta z_{k+1/2}, \qquad \tilde{v}_{i,j} = \sum_{k=1}^{K} v_{i,j}\Delta z_{k+1/2}.$$

The solution for $\tilde{u}_{i,j}^{n+1}$ and $\tilde{v}_{i,j}^{n+1}$ should be substituted into the continuity equation to obtain the final solution for sea surface topography. When we apply the boundary condition for vertical velocity at the surface and bottom ($w = 0$ at $z = 0$ and $z = \mathrm{H}$), the three-dimensional continuity equation will be reduced to a two-dimensional continuity equation.

The vertically integrated velocity components are obtained as follows:

$$\tilde{u}^{n+1} = \frac{1}{(l+T^2l^2)}\left[\frac{-2TgH}{R\sin\theta}(\delta_\lambda \bar{\zeta}^\theta)^n + \frac{2T^2\mathrm{lg}H}{R}(\delta_\theta \bar{\zeta}^\lambda)^n\right] + \bar{R}_\lambda, \tag{A20}$$

$$\tilde{v}^{n+1} = \frac{1}{(l+T^2l^2)}\left[\frac{-2TgH}{R}(\delta_\theta \overline{\zeta}^{\lambda})^n - \frac{2T^2lgH}{R\sin\theta}(\delta_\lambda \overline{\zeta}^{\theta})^n\right] + \bar{R}_\theta, \tag{A21}$$

where

$$\bar{R}_\lambda = \frac{1}{l+T^2l^2}\left[2T\sum_{k=1}^{K} R'_\lambda \Delta z_{k+1/2} - 2T^2l\sum_{k=1}^{K} R'_\theta \Delta z_{k+1/2}\right],$$

$$\bar{R}_\theta = \frac{1}{l+T^2l^2}\left[2T\sum_{k=1}^{K} R'_\theta \Delta z_{k+1/2} + 2T^2l\sum_{k=1}^{K} R'_\lambda \Delta z_{k+1/2}\right].$$

The vertically integrated velocity components should be substituted into the two-dimensional integral continuity equation to obtain the equation for sea surface topography. The two-dimensional integral continuity equation is written as follows:

$$\frac{1}{R\sin\theta}[\delta_\lambda \tilde{\bar{u}}^{\theta} + \delta_\theta \overline{\tilde{v}\sin\theta}^{\lambda}] = 0. \tag{A22}$$

Substituting Equations (A20) and (A21) into Equation (A22), we get the equation for sea surface topography for the internal grid points as follows:

$$\frac{1}{R\sin\theta}\left[\delta_\lambda\left(\overline{\frac{a}{R\sin\theta}\delta\lambda\overline{\zeta}^{\theta} - \frac{b}{R}\delta_\theta\overline{\zeta}^{\lambda}}^{\theta}\right) + \delta_\theta\left(\overline{\frac{a}{R}\delta_\theta\overline{\zeta}^{\lambda} + \frac{b}{R\sin\theta}\delta_\lambda\overline{\zeta}^{\theta}}^{\lambda}\right)\sin\theta\right] = R_s, \tag{A23}$$

where

$$a = \frac{2TgH}{(l+T^2l^2)}; \quad b = alT = \frac{2T^2gH}{(l+T^2l^2)}; \quad R_s = \frac{1}{R\sin\theta}[\delta_\lambda \bar{R}_\lambda + \delta_\theta(\bar{R}_\theta \sin\theta)].$$

The sea surface topography equation (A23) is solved by a successive overrelaxation technique. In fact, Equation (A23) can be solved by any one of the iterative methods. When the relaxation parameter is equal to 1.0, the successive overrelaxation method will automatically convert itself to the Gauss–Sidel iteration method. After 100 iterations, the maximum residual, $\max|\zeta^{n+1} - \zeta^{n-1}| \approx 10^{-5}$ cm (where n is the iteration number), has been achieved.

The numerical experiments were carried out using a supermini computer AViiON-4000 whose memory is 32 MB and the speed is 19 MIPS. The model is integrated for 60 days to get a steady state solution, which has taken about 15 h of computer time.

REFERENCES

1. A.S. Sarkisyan, 'Theory and calculations of ocean currents', Translation from US Department of Commerce and the National Science Foundation, Washington, DC, 1969.
2. R.P. Bulatov, Yu.L. Demin and S.G. Pogarkov, 'Surface topography of the Atlantic Ocean', *Oceanologia*, **6**, 995–1001 (1975).
3. Yu.L. Demin, 'A diagnostic calculation of currents in the tropical Atlantic', *Meteorologia i Hydrologia*, **1**, 48–57 (1975).
4. Yu.L. Demin, 'A non-linear baroclinic model and calculation of currents in the equatorial Atlantic', *Izv. Akad. Naukssr, Fir. Atmos. i. Okeana.*, **11**, 534–537 (1975).
5. G.L. Mellor, C.R. Mechoso and E. Keto, 'A diagnostic calculation of the general circulation of the Atlantic Ocean', *Deep-Sea Res.*, **29**, 1171–1192 (1982).
6. L.H. Kantha, G.L. Mellor and A.F. Blumberg, 'A diagnostic calculation of general circulation in the South Atlantic Bight', *J. Phys. Oceanogr.*, **12**, 805–819 (1982).
7. J.L. Sarmiento and K. Bryan, 'An ocean transport model for the North Atlantic', *J. Geophys. Res.*, **87**, 394–408 (1982).
8. A.S. Sarkisyan and Yu.L. Demin, 'A semi-diagnostic method of sea current calculation', Large-scale Oceanographic Experiments in the WCRP Publication Series, Tokyo, vol. 2(1), 1983, pp. 201–214.
9. G.I. Marchuk and A.S. Sarkisyan, *Mathematical Modelling of Ocean Circulation*, Springer, Berlin, 1988.

10. A.E. Gill, *Atmosphere–Ocean Dynamics*, Academic Press, New York, 1982.
11. Yu.L. Demin and R.A. Ibraev, 'A numerical method of calculation of currents and sea surface topography in multiply connected domains of the ocean', *Sov. J. Numer. Anal. Math. Model.*, **4**, 211–225 (1989).
12. J.D. Woods, 'The World Ocean Circulation Experiment', *Nature*, **314**, 505–511 (1985).
13. S. Hellerman and M. Rosenstein, 'Normal monthly wind stress over the world ocean with error estimates', *J. Phys. Oceanogr.*, **13**, 1093–1104 (1983).
14. S. Levitus, 'Climatological atlas of the world ocean', *NOAA Professional Paper 13*, US Government Printing Office, Washington, DC, 1982.
15. A.N. Cutler and J.C. Swallow, 'Surface currents of the Indian Ocean', *Report No. 187*, Institute of Oceanographic Sciences, UK, 8 pages, 36 charts, 1984.
16. D.R. Quadfasel and F. Schott, 'Southward subsurface flow below the Somali Current', *J. Geophys. Res.*, **88**, 5973–5979 (1983).
17. K. Wyrtki, *Oceanographic Atlas of the International Indian Ocean Expedition*, National Science Foundation, Washington, DC, 1971.
18. K. Wyrtki, 'An equatorial jet in the Indian Ocean', *Science*, **181**, 262–264 (1973).
19. R.L. Molinari, D. Olson and G. Reverdin, 'Surface current distributions in the tropical Indian Ocean derived from compilations of surface buoy trajectories', *J. Geophys. Res.*, **94**, 7217–7238 (1990).

